Faculty of Civil, Geo and Environmental Engineering
Chair for Computation in Engineering
Prof. Dr. rer. nat. Ernst Rank

Enforcement of Boundary Conditions in FCM with Applications to Biomechanics

Oguz Oztoprak

Master's thesis
for the Master of Science program Computational Mechanics

Author: Oguz Oztoprak

Supervisors: Prof. Dr.rer.nat. Ernst Rank
Dr.-Ing. habil. Stefan Kollmannsberger
Mohamed Elhaddad, M.Sc.
Lisa Hug, M.Sc.

Ausgabedatum: 01. November 2019
Abgabedatum: 31. March 2020

Acknowledgements

I would like to sincerely thank Mohamed Elhaddad for his continuous counsel, support and supervision. He challenged me to learn more and was very patient with me.

My sincere thanks go to Dr.-Ing. Stefan Kollmannsberger for introducing me to this project and his genuine interest in all aspects of this thesis, including my personal development.

I am grateful to have had John Jomo and Lisa Hug working next door, as they were always there to share some of their wisdom.

The great people in the chair for Computation in Engineering, Alexander Paolini, Davide D'Angella, Nina Korshunova, Philipp Kopp and the rest have been very friendly and supportive during our coffee breaks, my earnest thanks to them.

I would like to thank Prof. Ernst Rank for examining and supervising this thesis.

I would also like to thank Jan Kirschke, Amir Bayat and Tanja Lerchl from the spine imaging research group for their continuous support and counsel.

Special thanks to my friend Isinsu who listened to me talk, a lot and to my friend Özen for always being supportive.

Lastly, I want to express my deepest gratitude for my parent's support and unconditional love.

Contents

1 Introduction

1.1 Background and Context

The disruptions in the mechanics of the spine is among the primary causes of chronic back pain worldwide. Osteoporosis is a major cause of vertebral fractures, yet the recent advancements in diagnosis and treatment capabilities led the medical community to consider osteoporosis as treatable. On the other hand, no more than 15% of the relevant patients in EU receive adequate treatment [Fou04], suggesting that the modern diagnostic tools are not being utilized at their fullest potential. An early and accurate diagnosis is key to an effective treatment, therefore the research efforts taking advantage of the available medical tools to predict patient well-being is evermore critical. Among the challenges facing the timely diagnosis of vertebral fractures is the understanding of the complex mechanical aspects of the spine. The mechanical analysis of the vertebrae has the potential to make good use of the current medical imaging tools in an effort to generate key diagnostic insights.

Mechanical response of the spine largely depends on a complex relation between a series of vertebrae separated by intervertebral discs. The interaction of local effects, such as individual bone strength, and global effects, such as spinal alignment have direct influence on the structural well-being of the spinal vertebrae. Furthermore, the ligaments and muscles that support the alignment of the spine raise the complexity of the interaction. The nature of this interaction varies from patient to patient, making it infeasible to fit one biomechanical model to all patients. A natural approach to investigate the mechanical behavior of the spine is then to build patient-specific models. Moreover, transitioning from numerical simulations of a generic spine to a more individualized approach requires a significant

amount of automation to be of any practical use. The groundwork for establishing an automated workflow includes special treatment of geometry, loading and material properties in biomechanical models. The key idea is to build a numerical framework which can be fully automated, i.e. mindfully adopting numerical tools that can robustly handle varying geometry, loading and material conditions.

Geometrical models of the spine are often based on quantitative computed tomography (qCT) scanning, which is a widely adopted tool providing key material (e.g. bone mineral density) and geometry traits in the form of a 3D voxel representation [Ada09]. The standard methods for investigating mechanical behavior from qCT scans are mostly based on the classical Finite Element Method (FEM) [SYY+18, KRAA19]. Such investigations require an often cumbersome preprocessing phase including meshing and smoothing sharp geometrical features, which can involve manual labour. This preprocessing phase can take up to 20% of overall analysis time [CHB09]. For a patient-specific analysis, going through such preprocessing phase for each unique spine model is not practical and can impede automation efforts. By contrast, the Finite Cell Method (FCM) [PDR07] for voxel-based geometries is well suited to deal with complex voxel domains by simplifying the preprocessing phase. It can directly operate on the original geometry obtained from the qCT scan by utilizing the voxel structure and combining it with higher order finite elements in the spirit of fictitious domain approach [PDR07]. Considering the efficiency and robustness of FCM in handling voxel based geometries, it is apparent that this method is well aligned with the notion of automated personalized computation. Additionally, the capabilities of FCM in the context of femural bone simulation have been verified and validated, paving the way for adoption of the method in similar biomechanical settings [RTT+11].

The boundary conditions are another major aspect of numerical modelling and are especially critical in realistic modelling of the spine. The imposed constraints and loading conditions have a direct impact on the mechanical behavior of each vertebra. The nature of these boundary conditions is governed by the physical interaction of vertebrae that are stacked on top of each other. A Multi-body Simulation (MBS) can model this interaction by representing individual vertebrae with rigid bodies and the connecting intervertebral discs by non-linear spring-damper systems. By realistically modelling the movement and reproducing the induced loads on each vertebra from applied loads, the multi-body simulation serves the purpose of complimenting the static biomechanical model with necessary realistic boundary conditions. More specifically, in this thesis, a preceding MBS determines the loading and constraints to be imposed on each vertebrae, whereas the deformations are later computed with a separate biomechanical model based on the provided input.

Similar approaches combining two numerical methodologies to improve the combined analysis quality are often based on a combination of musculoskeletal dynamics and FE analysis. [MZZ+19] implemented a musculoskeletal inverse dynamic analysis to obtain the loading environment and built a patient-specific FEM model of femural cortical bone to analyze the mechanics of the bone after an endoprosthetic knee replacement. [LKNER18] and [LKAER18] approximated the loads by a musculoskeletal model of the upper body and applied the loads onto a FE model of the ligamentous

lumbosacral spine to study the effects of lumbo-pelvic rhythms on the mechanical response of the spine. [HAEvdB10] coupled a musculoskeletal model to a finite element model of the foot to allow for a more accurate prediction of stresses.

Regardless of the adopted method, proper application of the assumed boundary conditions remains a challenge as both the geometry and the boundary conditions can be arbitrarily complex. Within the context of a combined MBS and FCM approach, which is adopted in this thesis, these challenges originate from incompatible load types. Modelling the intervertebral discs as a spring-damper system in MBS gives rise to point-wise calculation of induced loads on each vertebra at the joints (i.e. point loads and moments). This simplification, however, does not hold true in reality, i.e. the whole end-plate surface of vertebra is under load, not a single point. Thus, a feasible strategy to apply point loads and moments onto the vertebral end-plates is required to ensure the credibility of the FCM model. Not only that, the strategy of choice should be in sync with the overall view of automating the computations on patient-specific qCT scans.

1.2 Goals

The overall vision that motivates this thesis is to provide a computational framework which facilitates a patient specific stress analysis in the spine under multiple realistic loading conditions. As part of the vision, this thesis commits to building a patient-specific computational model based on segmented vertebrae with minimal user intervention, where the boundary conditions stem from the multi body-simulation. The commitment entails the following steps.

1. The automatic generation of a finite cell grid from the segmented vertebra.
2. An automatic and accurate enforcement of Dirichlet boundary conditions onto the computational model.
3. An accurate transfer of loads from a multi-body simulation to a finite cell context.

The first step is handled by the non-boundary conforming finite cell grids considering the voxel geometry of the segmented vertebrae. By virtue of being an embedded method variant, the FCM is inherently well-suited for this step. The integration techniques tuned for voxel-based geometries are incorporated at this step [YRK+12]. The Dirichlet boundary conditions are handled by the automatic assessment of the input from the multi-body simulation. As a next step, the computed loads from the multi-body simulation is transferred to the finite cell setting by adopting the notion of material interfaces, where the discretization of a load transferring domain is weakly coupled with the discretization of a segmented vertebra. Hereby the joint loads calculated in the context of a multi-body simulation is accurately transferred to the segmented vertebra through the end-plate surfaces. The feasibility and robustness of the proposed computational approach is first verified by simple 3D examples, then investigated by taking a two lumbar vertebrae system.

A prerequisite to this goal is the thorough verification of the concept of the load transferring, to which a chapter of this thesis is dedicated. The assessment of various load cases on several geometries is performed to establish the credibility of the concept. Unlike the segmented vertebrae problem, where a tuned integration technique is well-suited, the examples use the octree integration to resolve the implicitly defined geometries [DR11].

1.3 Outline

The structure of this thesis is as follows. Chapter 2 starts with a basic overview of the FCM and builds on that foundation with the notion of imposing loads through a material interface. Additionally, the approximation of material properties from the qCT data is discussed. Chapter 3 provides three simple numerical cases aiming to show the capabilities of the proposed approach and verifying its accuracy. Next, Chapter 4 presents the basic governing principles of MBS and discusses its use case in conjunction with the FCM. The main numerical application area is introduced in Chapter 5, where a system with two vertebrae is analyzed and numerical results are discussed. Chapter 5 concludes with a preview of a more extensive four vertebrae system to demonstrate that the proposed workflow can be adapted for more realistic configurations.

2 Methodology

This chapter introduces the adopted methods to carry out a numerical analysis based on the data from the qCT scans. As a starting point, we first consider the relevant aspects of the Finite Cell Method along with a mathematical formulation of a model problem. The thesis then introduces a coupled material interface formulation in FCM. After building the necessary theoretical background, the application of material interfaces as a way to apply loads is introduced. As a final note, the interpretation of material properties from the qCT scans, with a special emphasis on vertebrae, is briefly discussed.

2.1 Basics of the Finite Cell Method

The Finite Cell Method (FCM) [PDR07] is variant of an embedded domain method that utilizes high-order shape functions to approximate a physical problem numerically. The principle motivation behind the development of FCM was to enable high order accurate numerical analysis on arbitrarily complex geometries without the hustle of generating a boundary conforming mesh. It aims to simplify numerical analysis by providing a modified workflow to the well-established Finite Element Method (FEM). FCM approaches the problem by extending the initial physical domain Ω_{phy} with an embedding fictitious domain Ω_{fict}, composing the overall computational domain $\Omega = \Omega_{\text{phy}} \cup \Omega_{\text{fict}}$. Since the fictitious domain has a simple geometry, it can be meshed without effort, creating a structured discretization of Ω composed of "cells" that contain both physical and fictitious parts. Moreover, the adoption of a high-order basis enables FCM to approximate the solution with high accuracy.

To recover the original problem on Ω_{phy}, the penalty parameter α is introduced such that:

$$\begin{aligned} \alpha(\boldsymbol{x}) &= 1.0 \quad \forall \boldsymbol{x} \in \Omega_{\text{phy}} \\ 0 < \alpha(\boldsymbol{x}) &\ll 1.0 \quad \forall \boldsymbol{x} \in \Omega_{\text{fict}} \end{aligned} \tag{2.1}$$

One possible interpretation of α is as a fictitious domain stiffness that introduces a modelling error. This modelling error, however, is shown to be bounded and accordingly FCM remains asymptotically consistent [DDR15]. It is a common practice to take α as a finite value close to 0 to ensure numerical stability.

Considering that the finite cells do not resolve the physical domain boundary, as shown in Figure 2.1, the FCM is not generally equipped with a basis that can meet the prescribed Dirichlet conditions strongly. More specifically, the solution vector does not contain entries whose linear combination can directly represent the values at the boundaries. An alternative way of enforcing Dirichlet conditions, which is used in this thesis, is the penalty method [Bab73]. The penalty method augments the weak field formulation and assigns a numerical penalty to the violation of the prescribed condition. The Nitsche method [JS09] is another well-established approach to this end.

The potential form of a linear elastostatic problem in FCM following the Minimum Total Potential Energy Principle [Red06] is introduced in Equation (2.2).

$$\delta\Pi_{int} + \delta\Pi_D = \delta\Pi_{ext}. \tag{2.2a}$$

$$\int_{\Omega} \alpha \cdot \boldsymbol{\sigma}(\boldsymbol{u}) : \delta\boldsymbol{\varepsilon}(\boldsymbol{u}) d\Omega + \int_{\Gamma_D} \beta_D \cdot (\boldsymbol{u} - \hat{\boldsymbol{u}}) \cdot \delta\boldsymbol{u} d\Gamma = \int_{\Omega} \alpha \cdot \boldsymbol{b} \cdot \delta\boldsymbol{u} d\Omega + \int_{\Gamma_N} \boldsymbol{t} \cdot \delta\boldsymbol{u} d\Gamma. \tag{2.2b}$$

$$\boldsymbol{\sigma} = \mathbb{C} \cdot \boldsymbol{\varepsilon}(\boldsymbol{u}) \tag{2.2c}$$

$$\boldsymbol{\varepsilon} = \frac{1}{2}\left(\nabla\boldsymbol{u} + \nabla\boldsymbol{u}^T\right) \tag{2.2d}$$

Where $\boldsymbol{u}$ is the displacement field, $\delta\boldsymbol{u}$ the variation of displacement field (also known as virtual displacement), $\delta\boldsymbol{\varepsilon}$ the variation of the strain tensor, $\mathbb{C}$ the elasticity tensor and β_D the penalty parameter. The fields $\hat{\boldsymbol{u}}, \boldsymbol{b}$ and $\boldsymbol{t}$ describe the prescribed Dirichlet values, the body forces and the surface traction respectively. The Principle of Minimum Total Potential Energy states that the analytical solution $\boldsymbol{u}^*$ renders $\Pi_{total}(\boldsymbol{u}) = \Pi_{int}(\boldsymbol{u}) + \Pi_{ext}(\boldsymbol{u})$ stationary [Fel04]. Application of this principle following standard techniques of variational calculus along with laws of linear elastic continuum results with Equation (2.2). Π_{int} is the total internal elastic energy stored in the system whereas Π_{ext} is the external energy due to applied mechanical forces. Inclusion of the penalty term is necessary to constrain the potential and ensure the uniqueness of the solution. This term, however, yields Equation (2.2) variationally inconsistent and the accuracy of the method in turn depends on the selection of β_D. For engineering purposes, such as the ones discussed in Chapter 5, the penalty approach delivers sufficiently accurate results and has the additional benefit of generalization to non-linear problems. Detailed analysis on practical implications of variational formulation with penalty

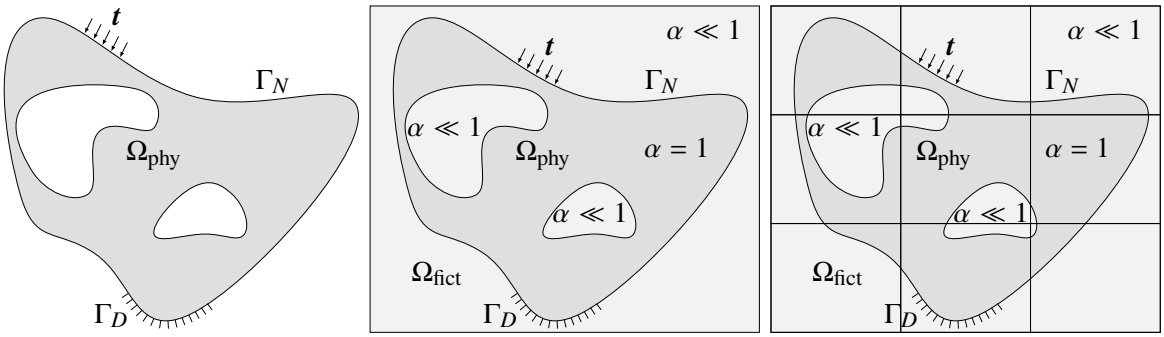

(a) Physical Domain **(b)** Extended FCM domain: $\Omega_{\text{phy}} \cup \Omega_{\text{fict}}$ **(c)** Cells composing the FCM mesh

Figure 2.1: Illustration of the Finite Cell Method

has shown that the optimal rate of convergence is recovered and the method is in most cases not too sensitive to the chosen penalty parameter [Bab73].

Equation (2.2) already incorporates α, determining which part of Ω contributes to the total potential energy of the system. In essence, the physical domain is considered only at the numerical integration of the bilinear form, as opposed to considering the geometry in the process of mesh generation. Consequently in FCM, the question of mesh quality is replaced with the need for efficient and accurate numerical integration schemes. The research on efficient numerical integration schemes for FCM is still on-going, and numerous approaches have been developed over the recent years [YRK+12] [KZKR16].

Additionally, the introduction of the embedding domain and the α parameter into the variational formulation has implications on the general convergence criteria of FCM. It is shown in [DDR15] that for $\alpha(\boldsymbol{x}) \rightarrow 0 \; \forall \alpha \in \Omega_{\text{fict}}$, FCM retains optimal convergence properties. Numerical studies in Chapter 3 further demonstrate the accuracy and convergence of FCM with the penalty approach.

2.1.1 FCM on voxel domains

The FCM approach to handle voxel domains from the qCT scans is similar to the more widely used Voxel Finite Element Method (VFEM). In the VFEM approach, each voxel represents an eight-node hexahedral element or several voxels form an element where the material property of the element is taken as the average of the assembled voxels. In FCM we have the similar flexibility of taking one or more voxels to form a cell while retaining the original material properties of each voxel, i.e. each cell can have piecewise constant material property. Therefore, FCM enjoys the additional flexibility of assuming as many/few voxels per element as numerically necessary without having to lose accuracy. After the appropriate selection of a voxel resolution, only a minor effort is required to generate a structured mesh. Efficient integration techniques tuned to voxel representations have been developed e.g. in [YRK+12].

2.2 Coupled formulation for embedded interface problems

The previous section introduced the FCM formulation and the workflow with one discretization scheme. For problems where interfaces separate subdomains with distinct material properties, using a global mesh to approximate the solution field results with non-ideal convergence rates [KOB+14] [EZB+17]. In this case, cells intersecting the material interface struggle to represent the kink in solution field across the interface. To retain attractive convergence properties in material interface problems, an alternative approach is adopted here, introduced in [Rue14]. Each subdomain is equipped with its own extended discretization, as in Figure 2.2, where the interface condition across subdomain boundaries is weakly enforced. A pure penalty approach is adopted to couple the FCM meshes. As a consequence, the formulation of a material interface problem requires an extension of the framework established in the previous section. More specifically, additional potential terms will be introduced in Equation (2.2) to account for the multiple meshes and the interface condition.

2.2.1 Embedded interface FCM model problem

The linear elastostatic model problem assumes a setting with two meshes and a single material interface across two sub-domains, as illustrated in Figure 2.2. A mathematical formulation analogous to the one presented in the previous section is as follows:

$$\delta\Pi^{(1)}_{int} + \delta\Pi^{(1)}_{D} + \delta\Pi_{inter} + \delta\Pi^{(2)}_{int} + \delta\Pi^{(2)}_{D} = \delta\Pi^{(1)}_{ext} + \delta\Pi^{(2)}_{ext}. \tag{2.3a}$$

$$\begin{aligned}\delta\Pi^{(1)}_{int} + \delta\Pi^{(1)}_{D} &= \int_{\Omega^{(1)}} \alpha \cdot \boldsymbol{\sigma}^{(1)}(\boldsymbol{u}^{(1)}) : \delta\boldsymbol{\varepsilon}^{(1)}(\boldsymbol{u}^{(1)}) d\Omega \\ &+ \int_{\Gamma^{(1)}_{D}} \beta^{(1)}_{D} \cdot (\boldsymbol{u}^{(1)} - \hat{\boldsymbol{u}}^{(1)}) \cdot \delta\boldsymbol{u}^{(1)} d\Gamma\end{aligned} \tag{2.3b}$$

$$\delta\Pi_{inter} = \int_{\Gamma_{inter}} \beta_C \cdot (\boldsymbol{u}^{(1)} - \boldsymbol{u}^{(2)}) \cdot (\delta\boldsymbol{u}^{(1)} - \delta\boldsymbol{u}^{(2)}) d\Gamma \tag{2.3c}$$

$$\begin{aligned}\delta\Pi^{(2)}_{int} + \delta\Pi^{(2)}_{D} &= \int_{\Omega^{(2)}} \alpha \cdot \boldsymbol{\sigma}^{(2)}(\boldsymbol{u}^{(2)}) : \delta\boldsymbol{\varepsilon}^{(2)}(\boldsymbol{u}^{(2)}) d\Omega \\ &+ \int_{\Gamma^{(2)}_{D}} \beta^{(2)}_{D} \cdot (\boldsymbol{u}^{(2)} - \hat{\boldsymbol{u}}^{(2)}) \cdot \delta\boldsymbol{u}^{(2)} d\Gamma\end{aligned} \tag{2.3d}$$

$$\delta\Pi^{(1)}_{ext} = \int_{\Omega^{(1)}} \alpha \cdot \boldsymbol{b}^{(1)} \cdot \delta\boldsymbol{u}^{(1)} d\Omega + \int_{\Gamma^{(1)}_{N}} \boldsymbol{t}^{(1)} \cdot \delta\boldsymbol{u}^{(1)} d\Gamma. \tag{2.3e}$$

$$\delta\Pi^{(2)}_{ext} = \int_{\Omega^{(2)}} \alpha \cdot \boldsymbol{b}^{(2)} \cdot \delta\boldsymbol{u}^{(2)} d\Omega + \int_{\Gamma^{(2)}_{N}} \boldsymbol{t}^{(2)} \cdot \delta\boldsymbol{u}^{(2)} d\Gamma. \tag{2.3f}$$

$$\boldsymbol{\sigma}^{(1)} = \mathbb{C}^{(1)} \cdot \boldsymbol{\varepsilon}^{(1)}(\boldsymbol{u}^{(1)}), \quad \boldsymbol{\varepsilon}^{(1)} = \frac{1}{2}\left(\nabla \boldsymbol{u}^{(1)} + \nabla \boldsymbol{u}^{(1)^T}\right) \tag{2.4a}$$

$$\boldsymbol{\sigma}^{(2)} = \mathbb{C}^{(2)} \cdot \boldsymbol{\varepsilon}^{(2)}(\boldsymbol{u}^{(2)}), \quad \boldsymbol{\varepsilon}^{(2)} = \frac{1}{2}\left(\nabla \boldsymbol{u}^{(2)} + \nabla \boldsymbol{u}^{(2)^T}\right) \tag{2.4b}$$

As each material domain has its own mesh, the internal and external energy associated with both domains naturally appear in the Equation (2.3) following superscripts (1) and (2). Similarly, Dirichlet boundary conditions of each domain are augmented into the potential formulation. The interface condition that "glues" the two meshes together appears in the formulation as $\delta\Pi_{inter}$. This contribution ensures that the displacement jump across the interface is penalized with the penalty factor β_C. Therefore, an appropriate choice of β_C serves to weakly impose the kinematic compatibility condition.

The formulation above ensures the C^0 continuity within each subdomain and more noteably, also allows for the C^0 continuity across the non-boundary conforming interface. Moreover, this approach with multiple meshes entails an additional surface mesh to perform the integration of the coupling terms along Γ_{inter}. The effort to generate such a surface mesh, nonetheless, is not as challenging as boundary conforming mesh generation for multiple subdomains.

2.3 Load transferring with embedded interfaces

This section discusses the application of point loads onto arbitrary boundary surfaces. The need for such an approach originates from the notion that point loads, in particular moments, can not directly be applied onto surfaces of arbitrary shape. Instead of a direct application of the equivalent distributed forces onto the Neumann surface, we employ a load transferring domain having a material interface with the physical domain. The load transferring domain has the following favorable properties that further justify its adoption.

1. It can assume the appropriate geometry and material properties.
2. It has a material interface with the original Neumann boundary surface of the physical domain, allowing the applied loads to be transferred as accurately as possible.

With this approach, the loads are applied onto the smooth surface of the load transferring domain and the coupling with the physical domain ensures that the effect of the applied load is distributed along the original Neumann surface. Figure 2.2 illustrates this idea, where an external moment M is to be applied on the physical domain $\Omega^{(1)}_{phy}$ through Γ^{orig}_N. The force couple $\mathbf{t_1}$ and $\mathbf{t_2}$ creates an equivalent moment on the load transferring domain $\Omega^{(2)}_{phy}$ along Γ^{new}_N and the embedded interface Γ_{inter} glues the two meshes. The mathematical formulations shown in Equation (2.3) governs the physical interaction.

Furthermore, the assigned stiffness for the supplementary domain plays an important role. It should not significantly effect the expected behavior of the physical domain while allowing for practical

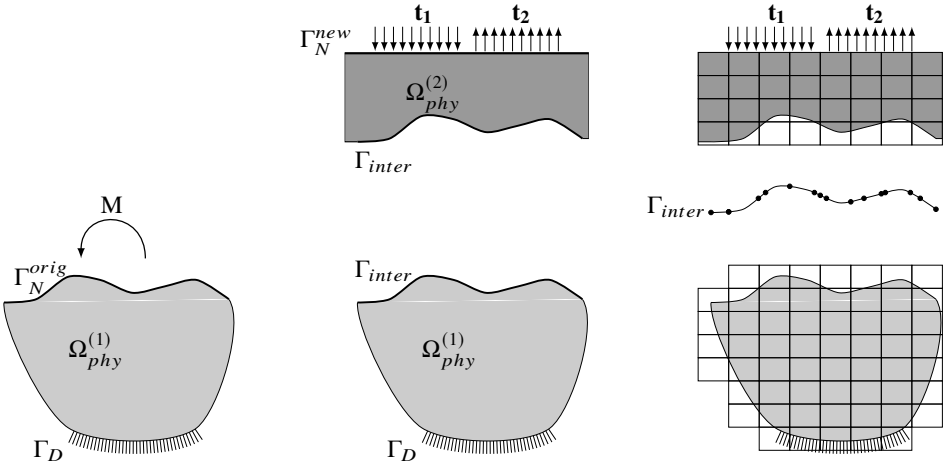

Figure 2.2: Illustration of load transferring with embedded interfaces. Force couple $\mathbf{t_1}$ and $\mathbf{t_2}$ producing an equivalent moment M.

application of various load cases. Numerical stability and the effect of elastic deformations of the load transferring domain on the overall behavior are key aspects requiring improved understanding. Therefore, additional numerical studies were conducted and compared with analytical solutions in Chapter 3 to verify various aspects of the proposed approach.

2.4 Assignment of material properties from the qCT scans

The qCT method can measure the bone mineral density (BMD) using a standard CT scanner with additional calibration to translate Hounsfield Units (HU) of the CT images to corresponding bone mineral density values [Ada09]. The BMD values, however, do not directly relate to the Young's Modulus (E), which is the material property of interest within the context of linear elastostatics. Thus, there is a need for a mapping between bone mineral density to the Young's modulus for each voxel. One well-established approach to estimate such mapping is as follows.

1. Obtaining an adequately large sample of bone specimens representative of the population.
2. Performing qCT scans to obtain the BMD value of each bone specimen.
3. Performing mechanical experiments on the bone specimens and determining the Young's modulus.
4. Determining the relationship between BMD and E using a regression analysis.

The above procedure naturally has to be carried out for each type of bone on which an internal deformation analysis is intended, as not all bones have similar properties. The specific application area of interest in this thesis is the biomechanics of the spine for which appropriate maps exist. Kopperdahl et al. [KMK02] followed a similar approach as in above, to arrive at linear and power law models for vertebrae. The following linear model from [KMK02] correlating BMD to E is adopted

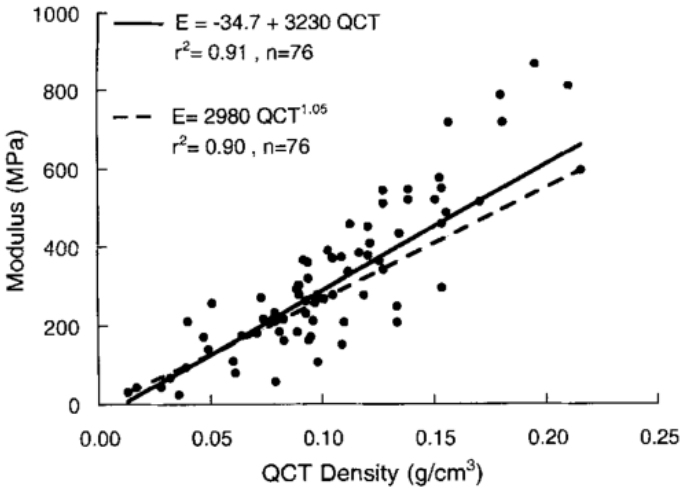

Figure 2.3: The linear and power law models resulting from the regression analysis, taken from [KMK02]. The linear model, shown in solid line, is used in this thesis.

for applications in Chapter 5.

$$E = -34.7 + 3230\,\mathrm{BMD} \tag{2.5}$$

In Equation (2.5), E is in MPa and BMD is in g/cm^3. The adopted linear model is based on a sample of size n = 76 and has a R^2 value of 0.91 as depicted in Figure 2.3.

It is important to note that the proper estimation of the Young's moduli has a direct influence on the accuracy of the numerical analysis. On the other hand, neither the CT scan specific calibration from Hounsfield Units to BMD nor the modelled correlation between BMD and E is without errors. Nevertheless, the introduced modelling error is assumed to be negligible as compared to the other sources of errors in this biomechanical application.

3 Verification

This chapter presents three basic numerical examples illustrating the solution characteristics of material interfaces as a way of indirect load application. The main goal of this chapter is to investigate the feasibility of the proposed approach within the context of 3D linear elasticity. The examples were chosen on the basis of having similar boundary conditions as a vertebra and possessing analytical solutions. Three fundamental load cases are considered, namely a twisting moment, a bending moment and an axial load. To compute the error of the proposed approach, reference FCM solutions along with the known analytical solutions are used e.g. displacements and relevant stresses. The Poisson's ratio ν was set to 0 for all cases. The integration for the cylindrical geometries were performed by an octree approach, where application of the recursive sub-division of the finite cells that are cut by the boundary results in an octree of integration sub-cells (quadtree in 2D), illustrated in Figure 3.1 [SRZ+12]. All computations were performed with the in-house code AdhoC++ of the chair for Computation in Engineering (CIE) at TUM. The Intel® MKL Pardiso direct solver was used to solve the underlying system of equations [Int20].

3.1 Clamped cylindrical beam

3.1.1 Problem setup

The first numerical case is a cylindrical beam with length l and radius r, clamped on one end and under torsional moment on the other end as shown in Figure 3.2. This simple problem in linear elasticity

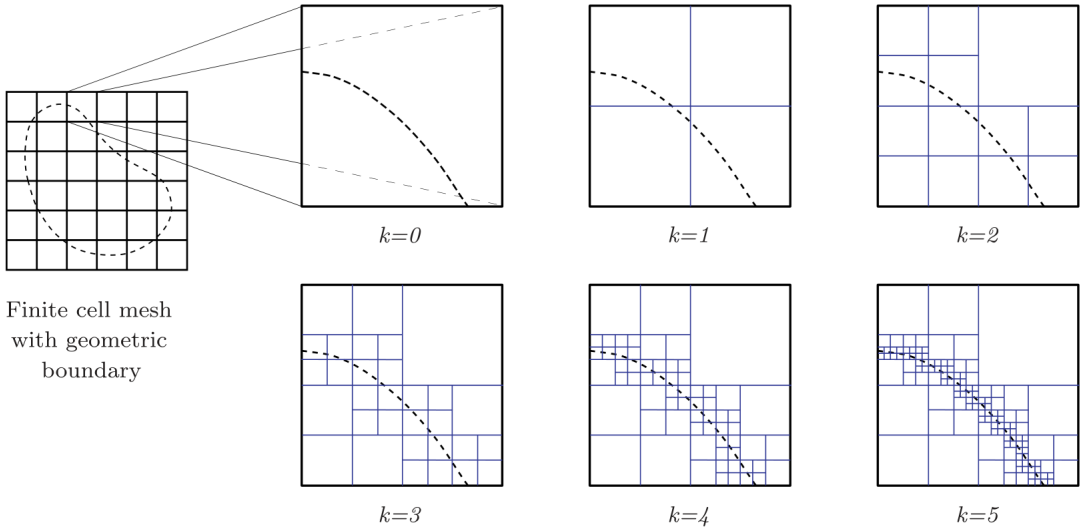

Figure 3.1: Recursively partitioned sub-cell structure in 2D. Subdivided cells are shown with blue lines and geometric boundary is shown with dashed lines. The resulting tree depth is represented by k [SRZ+12].

has a well-known analytical solution, which is introduced next in terms of the angle of twist and the shear stress.

The shear stress developed at a radial distance d from the cylindrical section reads as follows [AF11].

$$\tau = \frac{\mathrm{T}\, d}{J} \tag{3.1}$$

In Equation (3.1), the total applied torque is represented by T and J is the polar moment of area. For a circular cross-section, the polar moment of area reads:

$$J = \iint_A r^2 \, dA = \int_0^{2\pi} \int_0^R r^2 \, (r \, dr \, d\theta) = \frac{\pi R^4}{2} \tag{3.2}$$

From Hooke's law and considering the assumption of small displacements in linear elasticity, the angle of rotation is found as follows.

$$\Phi = \frac{\mathrm{T}\, l}{G J} \tag{3.3}$$

The shear modulus is shown as G in Equation (3.3). An evident consequence of applying pure torsion is that only shear stresses are present, which depend linearly on the radial distance from the center of the section.

Pure tension was considered as an additional independent load case, depicted in Figure 3.3. The analytical solution in terms of the normal stress and the displacement for this load case reads as

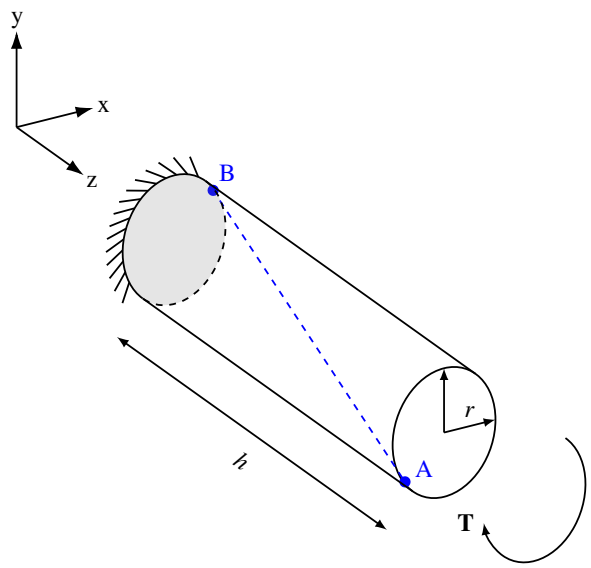

$$E = 3.52 \times 10^8 \frac{N}{mm^2} \qquad h = 6\,mm \qquad r = 1\,mm$$

$$\nu = 0.0 \qquad G = 1.76 \times 10^8 \frac{N}{mm^2} \qquad \mathrm{T} = 3.14 \times 10^4\, N \cdot mm$$

Figure 3.2: Clamped cylindrical beam under pure torsion.

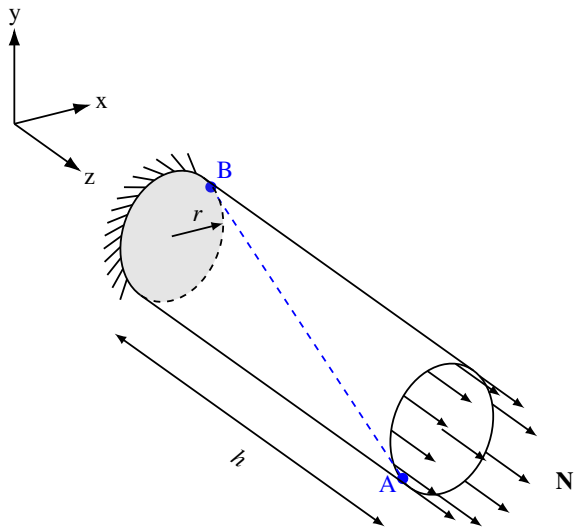

$$E = 3.52 \times 10^8 \frac{N}{mm^2} \qquad h = 6\,mm \qquad r = 1\,mm$$

$$\nu = 0.0 \qquad \mathrm{N} = \pi \times r^2 \times 20000 \frac{N}{mm^2} = 6.28 \times 10^4\, N$$

Figure 3.3: Clamped cylindrical beam under pure axial load.

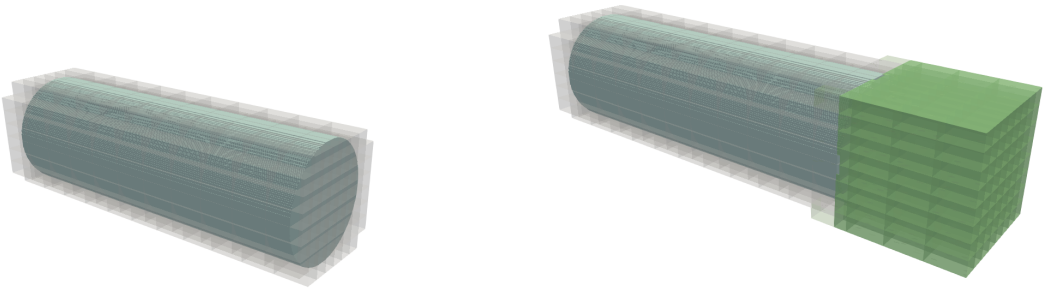

(a) The discretization of the reference FCM approach.

(b) The two discretizations of the proposed FCM approach.

Figure 3.4: FCM discretizations of cylindrical beam examples

follows.

$$\delta = \frac{\mathrm{N}\, l}{A\, E} \tag{3.4a}$$

$$\sigma = \frac{\mathrm{N}}{A} = \frac{\delta\, E}{l} \tag{3.4b}$$

In Equation (3.4a), the total applied normal force is represented as N, the axial deflection in z direction as δ, distance in z direction from the clamped end as l, the elastic modulus as E and the cross-sectional area as A. As the applied axial load, the cross-sectional area and the elastic modulus is constant, the stress, by definition, is constant everywhere. The displacement, on the other hand, changes linearly. The maximum displacement is at the load surface and the displacement is zero at the clamped end.

In the FCM studies investigating the configurations depicted in Figures 3.2 and 3.3, the beam was embedded into a $2 \times 2 \times 12$ finite cell discretization. The cells that are cut by the cylinder boundaries are further partitioned during the octree integration with a tree depth $k = 7$. The left and right circular boundary surfaces are generated as a surface triangulation using the Visualization Toolkit (VTK) [Kit20] and the resulting triangulations were intersected with the finite cell grid to further partition the surface triangulation, ensuring a more accurate integration. The Dirichlet condition was weakly enforced with a penalty $\beta_D = 10^{16}$ whereas the α coefficient was fixed to be 10^{-12}. Two FCM studies per numerical case were conducted: a reference FCM with one mesh and a FCM with material interfaces and coupled meshes. The same octree integration with a tree depth of $k = 7$ was employed for the secondary load transferring mesh. The penalty parameter for coupling of the meshes across the right end surface of the beam were chosen as $\beta_C = 10^{13}$. The numerical experiments were conducted with polynomial degrees $p \in \{2, 3, 4\}$. The elastic modulus of the load transferring domain was chosen as $E_{\text{load-trans}} = 10^7\, E_{beam}$, making the domain almost rigid compared to the beam.

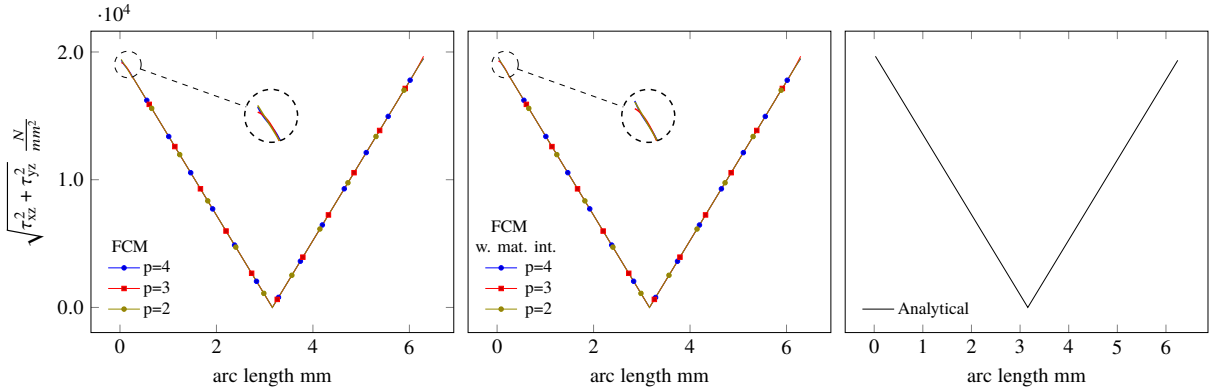

Figure 3.5: Comparison of the resulting shear stresses along the line A-B under pure torsion.

3.1.2 Numerical results and solutions

A representative line from point A to B, as in Figures 3.2 and 3.3, was established to investigate the accuracy of the proposed approach. Figures 3.5 and 3.6 illustrate the change in shear stress and displacement from point A to B, respectively. The notion of primary variables, e.g. displacements, being computed with greater accuracy than derived quantities, e.g. stresses, is well-established and documented. This tendency can be attributed to the fact that the unknowns in the linear system of equations are the displacements and stresses are derived from the displacements [Fel04]. With this notion in mind, Figures 3.5 to 3.8 can be better interpreted.

Figure 3.6 illustrates that under the pure torsion load case, the FCM with load transferring interface agrees with the analytical solution, with the difference in L2 norm being less than 0.1% for displacements across all polynomial degrees. Figure 3.5 depicts the magnitude of the computed shear stresses along the arc length of the beam. Larger perturbations of approximately 0.5% can be observed near points A and B. These differences occur only near the boundaries and dissipate away from it, thus the effect can be attributed to the presence of the boundary conditions. A remedy that is often used to increase the accuracy in such circumstances is the multi-level local hp refinement [Zan17]. For the sake of simplicity, such refinement strategies were not used, nevertheless numerical studies have previously shown the capabilities of the multi-level hp refinement in similar cases [Zan17, EZB+17]. The use of an integration approach better suited for circular geometries, such as the smart octree integration [KZKR16], is another approach that could minimize the observed perturbations. For the purposes of verification, however, it can be concluded that the proposed approach in Figure 3.4b with coupled meshes results in almost identical stresses as compared to the reference FCM approach shown in Figure 3.4a with a single mesh. Hence, the accuracy of the multi mesh approach is verified for this setting.

The interpretation of the axial load case is similar to the pure torsion. Figure 3.8 illustrates that for all polynomial degrees the displacements are captured well by the proposed approach, within 0.1% of the analytical displacements in L2 norm. The normal stresses in Figure 3.7 show variations from the

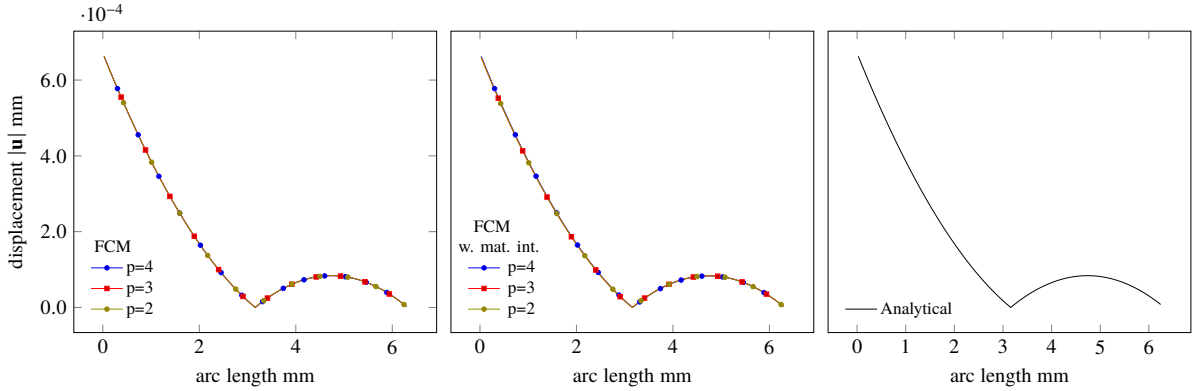

Figure 3.6: Comparison of the resulting displacements along the line A-B under pure torsion.

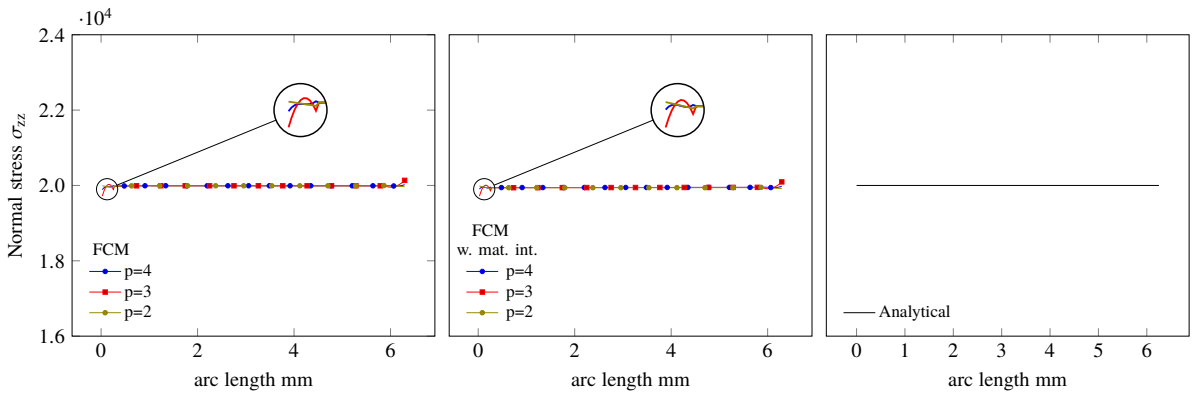

Figure 3.7: Comparison of the resulting normal stresses along the line A-B under pure axial load.

analytical stress near the boundary regions. The maximum deviation of the normal stress, however, was observed to be under 1%. The key take away is that the observed disruption of stresses near the boundary can be remedied by the multi-level hp refinement and the smart octree integration techniques as mentioned above. To sum up, the deviations in normal stress shown in Figure 3.7 are small and the numerical results of the proposed multi mesh approach can be considered as credible for this configuration.

3.2 Clamped rectangular beam

3.2.1 Problem setup

A cantilever beam with a rectangular cross-section was chosen to study the application of bending moments with the proposed approach. Figure 3.9 presents the problem statement, where the bending around the x axis is applied on the right end surface. Due to the applied bending moment, the areas below the Neutral Axis (N.A) are under compressive stress and the areas above N.A are under tensile stress. The analytical equations describing the deformation and normal stress on slender, linear elastic

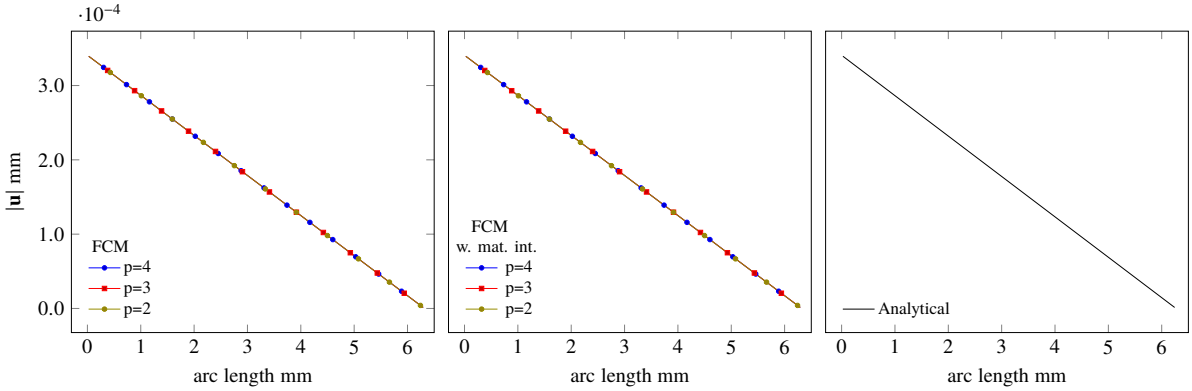

Figure 3.8: Comparison of the resulting displacements along the line A-B under axial load.

beams due to bending are well-known and shown as follows [AF11, GT99].

$$\sigma_b = \frac{\mathrm{M\,y}}{I} \tag{3.5}$$

Equation (3.5) is known as the "flexural formula", where σ_b is the developed normal stress due to bending, y is the distance from the N.A and I is the second moment of area. The flexural formula asserts that for a constant cross-section under a static moment, the normal stress due to bending only depends on the perpendicular distance from the N.A. The planar second moment of area with regard to x axis for a rectangular cross section with width t and height b can be found as in Equation (3.6).

$$I_x = \iint_A y^2 \, dA = \int_{-\frac{t}{2}}^{\frac{t}{2}} \int_{-\frac{b}{2}}^{\frac{b}{2}} y^2 \, dy \, dx = \frac{t\,b^3}{12} \tag{3.6}$$

The deflection formula corresponding to Equation (3.5) for a cantilever beam under pure bending, is as follows.

$$\delta_y = \frac{\mathrm{M}\,z^2}{2\,EI} \tag{3.7}$$

Equation (3.7) specifies that the deflection at any point on the beam is squarely proportional to the perpendicular distance z from the clamped end. The formula is based on the moment-curvature relationship and the small displacement assumption, where the successive integration of the moment-curvature equation considering the clamped boundary conditions results in Equation (3.7) [AF11, Buc04]. Note that the load case is pure bending without any shear force. As a result no shear deformations are present and the underlying assumption of plane sections remaining plane is satisfied. More specifically, the above theory holds for the configuration depicted in Figure 3.9 even though the beam has a relatively high slenderness ratio of $b/h = \frac{4}{10}$, as there is no shear deformations [Neg00, AF11].

The geometry depicted in Figure 3.9 was discretized by $2 \times 4 \times 10$ finite cells, which matched the boundaries of the rectangular beam exactly. Consequently, the integration was performed using

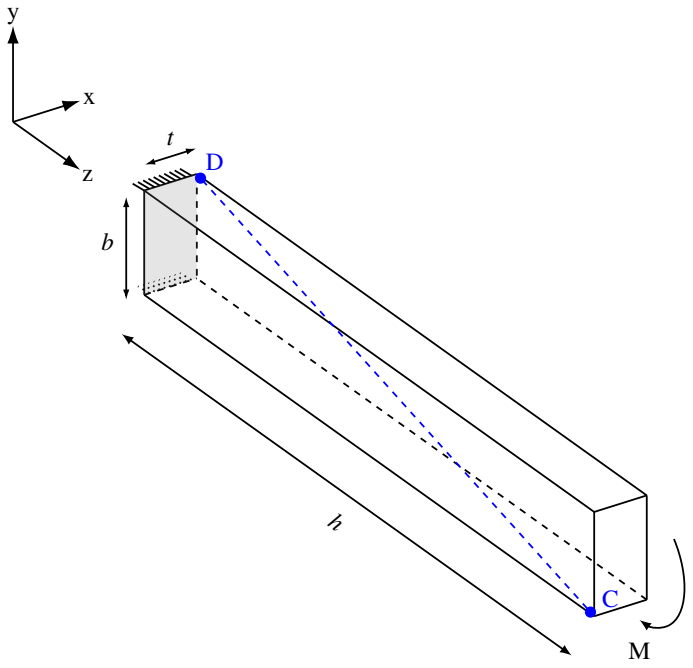

$E = 3.52 \times 10^8 \frac{N}{mm^2}$ $h = 10\,mm$ $b = 4\,mm$

$t = 2\,mm$ $\nu = 0.0$ $\mathrm{M} = 2.13 \times 10^7\, N \cdot mm$

Figure 3.9: Clamped cylindrical beam under pure bending on xy plane

a conventional Gauss-Legendre quadrature [PDR07]. Thus, for this particular geometry the FCM approach resembles the standard p-FEM, as the finite cells can represent the geometry exactly. The weak Dirichlet condition was enforced with a penalty of $\beta_D = 10^{16}$ and the α coefficient was chosen as 10^{-12}. The coupling penalty parameter β_C was chosen to be 10^{13}. The load transferring domain was deliberately designed to have a larger cross-section than the physical domain to make sure that the size of the helper domain is not a relevant factor, as long as it encloses the coupling surface. Similar to the setup in Section 3.1.1, the stiffness of the load transferring domain was taken as seven orders magnitude stiffer than of the physical domains'.

3.2.2 Numerical results and solutions

The illustration of the numerical results for the cantilever rectangular beam strictly follows the procedure in Section 3.1.2. Comparison of deflections and normal stresses are carried out along a representative line from C to D, as shown in Figure 3.9.

The deflections in y direction, u_y, along the cutting line C-D are shown in Figure 3.11. The deflections u_y computed by the two meshed FCM approach have an error bounded by 0.1% compared to the analytical solution. The result shows accordance with the outcome of the previous cases in Section 3.1.2.

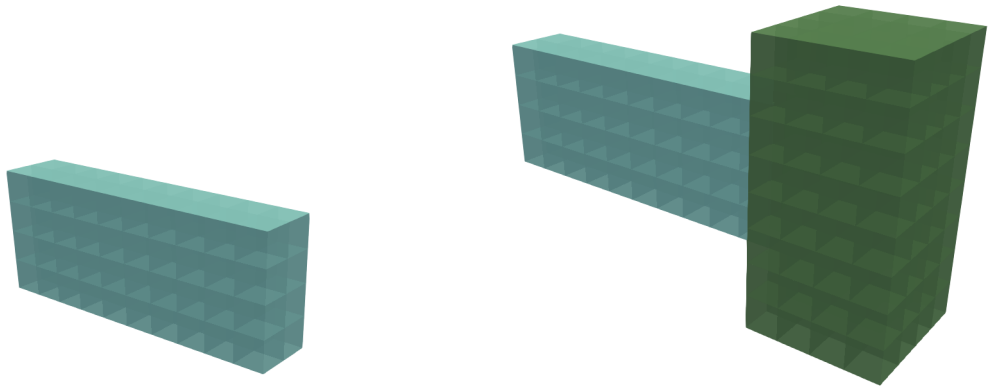

(a) The discretization of the reference FCM approach.

(b) The two discretizations of the proposed FCM approach.

Figure 3.10: FCM discretizations of rectangle beam example

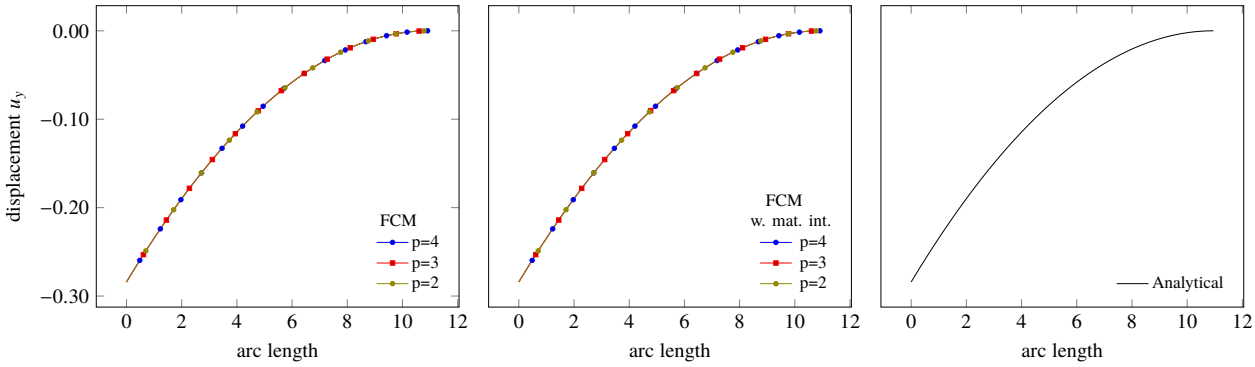

Figure 3.11: Comparison of the resulting displacements along the line C-D under pure bending.

The absolute values of the normal stresses σ_{zz} along the cutting line C-D are considered in Figure 3.12. Similar to the deflections, the proposed multi mesh method approximates the stresses with an error less than 0.1% compared to the normal stresses calculated from Equation (3.5). The discretization in this particular case could represent the geometry exactly, therefore the stresses were captured with a greater accuracy compared to the cylindrical beam examples, specifically around the boundary region. This observation supports the argument that a more accurate integration on the cylindrical beam examples could properly resolve the stresses near the boundaries.

3.3 Minimally restrained cylindrical beam

3.3.1 Problem setup

The last numerical case considers a slender cylindrical beam with its rigid body modes disabled. We apply equal and opposite torques from each side as shown in Figure 3.13. The key aspect that makes

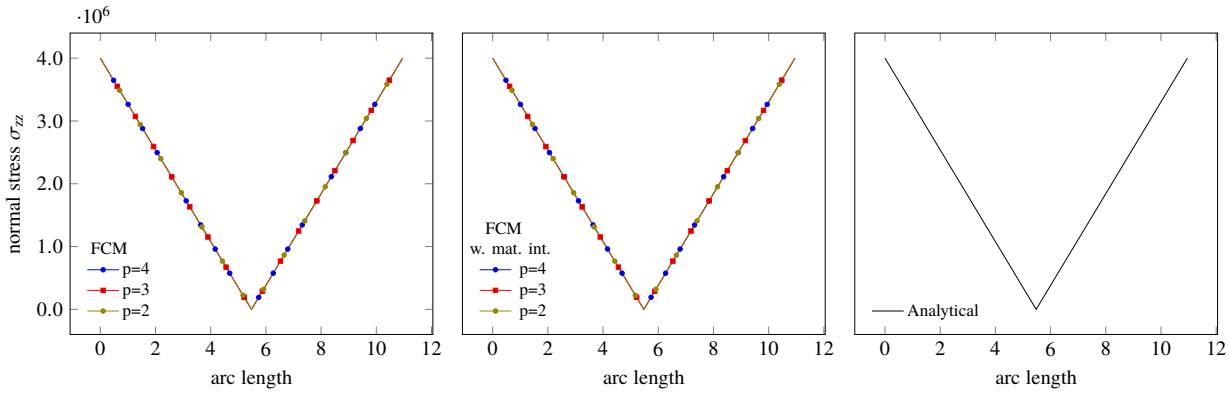

Figure 3.12: Comparison of the resulting normal stresses along the line C-D under pure bending.

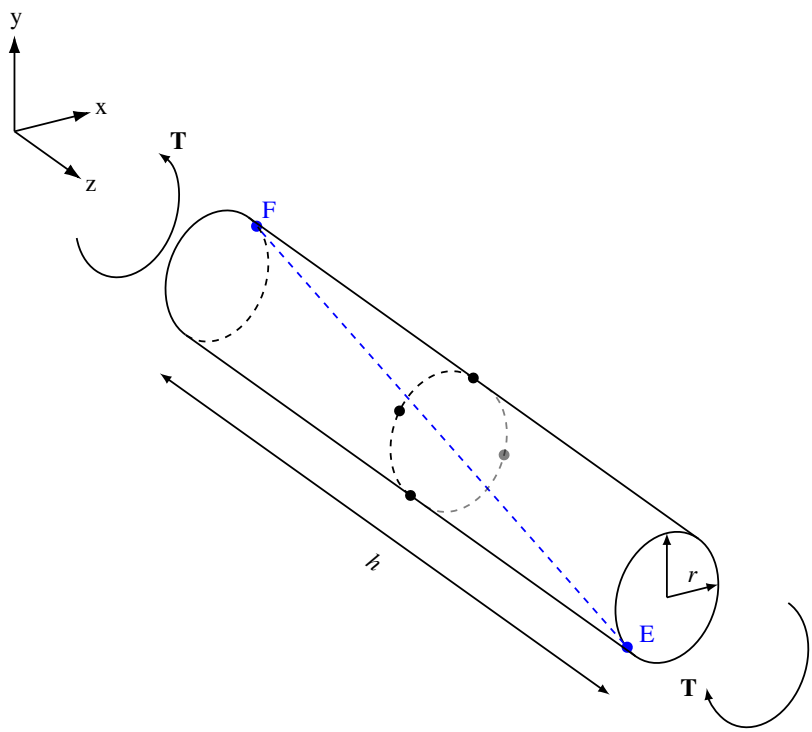

$$E = 3.52 \times 10^8 \frac{N}{mm^2} \qquad h = 10\,mm \qquad r = 1\,mm$$

$$\nu = 0.0 \qquad G = 1.76 \times 10^8 \frac{N}{mm^2} \qquad \mathrm{T} = 31415.927\,N \cdot mm$$

Figure 3.13: Point-wise restrained cylindrical beam under pure torsion.

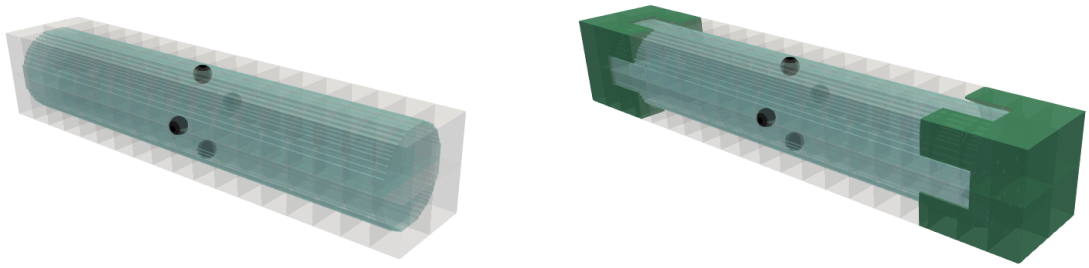

(a) The discretization of the reference FCM approach.

(b) The two discretizations of the proposed FCM approach.

Figure 3.14: FCM discretizations of minimally restrained cylindrical beam example.

this case unique is that the external loads alone are in equilibrium, i.e. no reaction forces are expected at the supporting points. The Dirichlet conditions are deliberately enforced in such a way to only eliminate the rigid body motion. From the computation point of view, the stiffness matrix without any Dirichlet conditions is singular and the term "minimally restrained" is referring to restraining minimal number of degrees of freedom to ensure the invertibility of the stiffness matrix.

The unique aspect of this example is the application of loads from both ends of the beam, featuring two load transferring domains to realize it, as shown in Figure 3.14. This specific configuration is vital to verify, as a fundamentally similar configuration will be used in Chapter 5.

The governing analytical equations in Equations (3.1) to (3.3) are employed to compare the accuracy of the considered numerical approach.

A discretization of $2 \times 2 \times 20$ was carried out in both of the FCM studies. Similar to the first numerical case in Section 3.1, the octree depth was chosen as $k = 7$, weak Dirichlet penalty parameter β_D was set to 10^{16}, α coefficient was fixed to 10^{-12} and the material interface penalty parameter β_C was set to 10^{13}. The Young's modulus of the load transferring domain was set to $E_{\text{load-trans}} = 10^7 \, E_{beam}$ to stay consistent with the previous sections. The study considered polynomial degrees of $p \in \{2, 3, 4\}$ where the displacements and shear stresses on the virtual line E-F were computed and compared with analytical results.

3.3.2 Numerical results and solutions

Figures 3.15 and 3.16 depict the resulting displacements and shear stresses along the E-F line. The displacements computed by the proposed method approximate the analytical solution with an error of less than 0.1% in L2 norm. This behavior validates the observations in the previous sections with respect to the achievable accuracy in the displacements.

The case for shear stresses follows the arguments in Section 3.1.2. The L2 norm of in-plane shear stresses were computed to have a difference of less than 0.5% compared to the analytical shear stresses. Similar to previous cases, most of the variations in stresses are observed locally near the ends

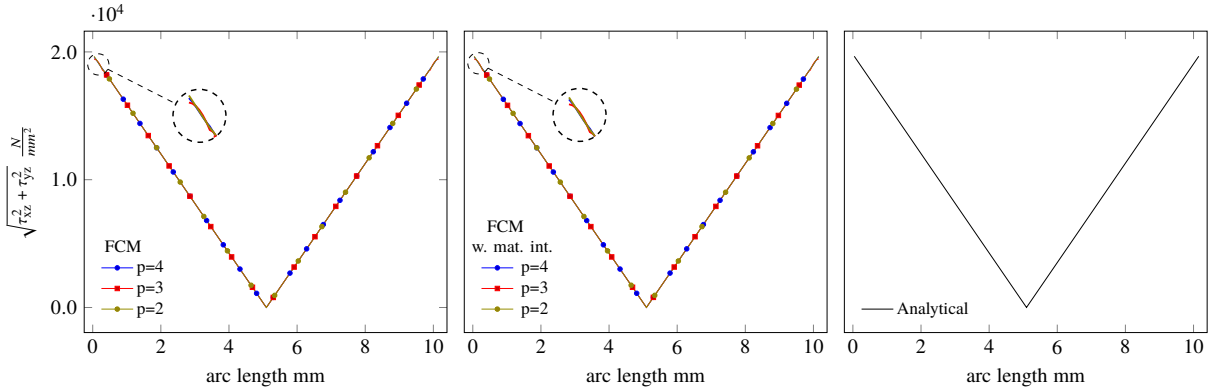

Figure 3.15: Comparison of the resulting shear stresses along the line E-F under pure torsion.

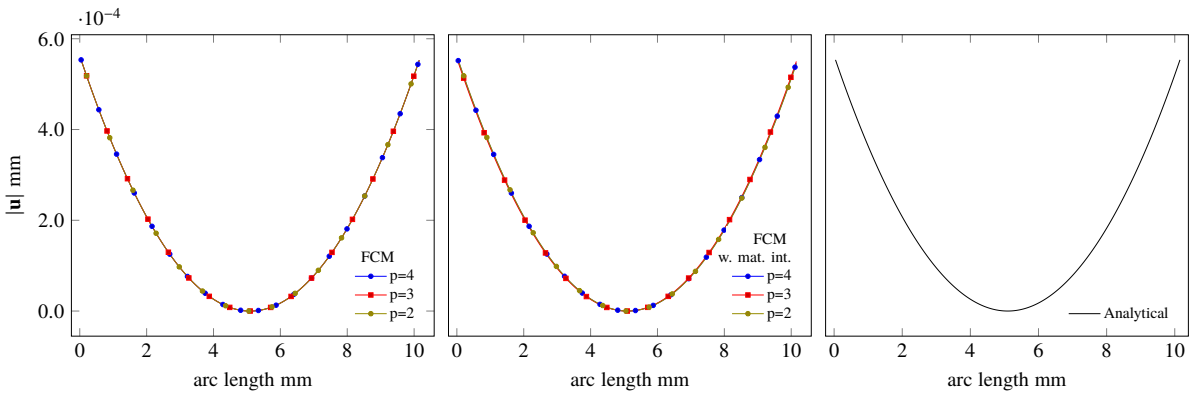

Figure 3.16: Comparison of the resulting displacements along the line E-F under pure torsion.

of the beam, as illustrated in Figure 3.15. Note that the strategies to improve the approximation of stresses discussed in Section 3.1.2 also apply for this case. Moreover, the L2 norm of the out of plane shear and the axial stresses at the restrained Dirichlet points were observed to be less than $20\frac{N}{mm^2}$. Considering that the L2 norm of the torsional stresses at the surface of the beam are approximately $2.0 \times 10^4 \frac{N}{mm^2}$, the observed artificial stresses can be considered small. In an ideal scenario, only in-plane shear stresses would be present under the specified loading. The cause of the non-physical stresses can be speculated to be the inexact enforcement of the Dirichlet conditions. A more thorough study eliminating the integration errors could reveal the underlying cause. On the other hand, this observation supports that the minimal restraint mostly did not restrain any internal deformation modes, as the observed non-physical stresses are small compared to the applied load. For our purpose of verification, the numerical results boost confidence in the proposed method and its potential adoption in more complex systems.

Even though the considered selection of configurations were simple in nature, they covered the basic set of boundary conditions that are especially critical in a workflow combining MBS and FCM. Although the observed errors near the boundary regions remain to be further investigated, we consider the proposed methodology to be verified since these errors consistently remained below other expected sources of errors (e.g. the real loading conditions).

4

Combined analysis with multi-body dynamics

We start this chapter by an overview of the multi-body systems and the generalized governing equation of motion used to solve such systems. In the second part, we study the important aspects of the combined analysis of multi-body dynamics and linear-elastostatics. Finally, the underlying assumptions that allow for such a combined approach are discussed.

4.1 Basics of multi-body dynamics

A multi-body system (MB system) has one or more connected rigid bodies, where the connecting elements between the bodies and the environment can be massless springs, dampers, joints and possibly others, as shown in Figure 4.1. A multi-body simulation (MBS) studies how the MB system moves under certain loads, i.e. starting from an initial configuration at t_0, it computes the new position, velocity and acceleration of its elements at later time steps. The linearized equation of motion allowing the treatment of the mechanical behaviour of a general MB system is presented as follows [Bay94, Wit08].

$$\mathbf{M}\,\ddot{\mathbf{q}}(t) + \mathbf{C}_{\mathbf{q}}^{T}\,\boldsymbol{\lambda} + \mathbf{D}\,\dot{\mathbf{q}}(t) + \mathbf{K}\,\mathbf{q}(t) = \mathbf{F}(t) \tag{4.1a}$$

$$\mathbf{C}\,(\mathbf{q}, \ddot{\mathbf{q}}) = \mathbf{0} \tag{4.1b}$$

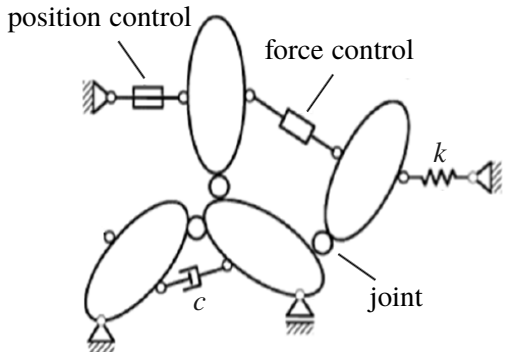

Figure 4.1: A generic MB system with various components [VdJDA+13].

The generalized coordinates are denoted by $\mathbf{q}$, where $\mathbf{q} = [\mathbf{x} \quad \boldsymbol{\Psi}]^T$ is one possible definition with $\mathbf{x}$ as the translational degrees of freedom and $\boldsymbol{\Psi}$ as the rotational degrees of freedom. $\mathbf{M}$ represents the mass matrix describing how the material is distributed within the rigid bodies. The constraint conditions are represented by $\mathbf{C}$ and $\mathbf{C}_{\mathbf{q}}^T$ is the derivative of the constraint conditions with respect to $\mathbf{q}$. The constraints often represent an applied loading on constraint degrees of freedom without changing the potential energy of the body and the coefficients $\boldsymbol{\lambda}$ represent the loading magnitude. $\mathbf{K}$ and $\mathbf{D}$ are the stiffness and damping matrices, respectively, where these matrices capture the nature of the connection between the rigid bodies, i.e. the way they interact with each other. Finally, $\mathbf{F}$ denotes the force vector. Note that depending on the type of non-linearity, the matrices appearing in Equation (4.1) could additionally be a function of $\mathbf{q}$ or $\dot{\mathbf{q}}$.

By solving the Equation (4.1) at each time step, we can compute the force or the moment each component exerts on the bodies as a function of time. In essence, multi-body simulations allow us to first set up a system of interconnected rigid bodies with the surrounding environment and then to compute the trajectory and load state of the bodies in time.

4.2 Quasi-static analysis and assumptions of combined approach

One case that significantly simplifies the interpretation of the MBS results is when the accelerations, $\ddot{\mathbf{q}}$, remain small, i.e. the dynamic forces generated from accelerations can be neglected. In this case, spring and damper elements absorb most of the applied force. Therefore, the equilibrium can be maintained, in an approximate sense, even if the dynamic forces generated by accelerations are neglected. Viewed from the perspective of the computation of internal deformations, the equilibrium of the system at each time step is crucial as a non-physical load case likely produces strictly non-physical internal deformations. In other words, in case small accelerations are observed in a MBS, a supplementary analysis considering linear elastostatic analysis is still a good approximation of the dynamic system. To sum up, a linear elastic analysis that relies on MBS to approximate the loading state can be used in case the accelerations are small. Within the context of engineering applications,

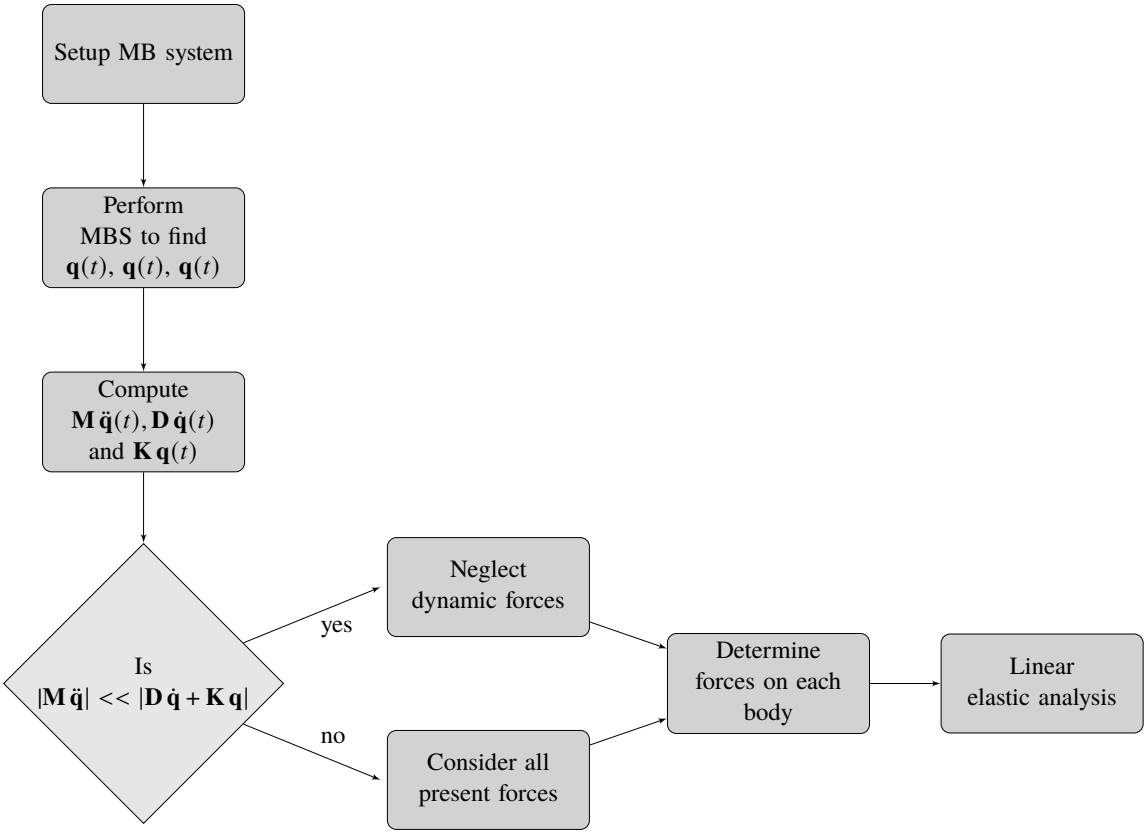

Figure 4.2: Flow chart demonstrating the steps of MBS leading to its association with linear elastic analysis.

if the forces induced by accelerations contribute no more than 1% of the total forces, we can safely assume that accelerations are negligible. A flow chart in Figure 4.2 depicts the discussed workflow.

Another assumption that requires attention is the negligence of internal deformations during the MBS. More specifically, the MBS do not consider the bodies as deformable but as rigid bodies. This assumption mostly holds in case the bodies have significantly higher stiffness than the interconnecting springs. In such cases, the equivalent stiffness of a body with a connected spring could be assumed as merely the stiffness of the spring. A system modelling the interactions of vertebrae can make such an assumption as the springs representing the behavior of intervertebral discs have sufficiently smaller stiffness than of the vertebral bodies.

5 Applications on vertebrae

As the FCM with weak coupling and combined analysis with MBS was discussed, we demonstrate the applicability of using a stiff load transferring domain as means to apply loads in a combined MBS and FCM analysis of multiple vertebrae. The software Simpack [Das20] was used to perform the MBS and the in-house high-order FEM framework AdhoC++ was used to carry out the FCM simulations. The MBSs were performed by Tanja Lerchl, a doctorate student working in cooperation with the Associate Professorship of Sport Equipment and Sport Materials at TUM. We consider a two vertebrae model as an example, where the intervertebral discs (IVDs) and the vertebral bodies are modeled. Within the context of this thesis, the effects of the muscles and the ligaments on the mechanical behavior of the vertebrae are not considered. The two vertebrae system can easily be extended to several vertebrae for a more realistic scenario. Such an extension is a natural starting point for further research in this area, thus a more comprehensive system is briefly introduced in Section 5.5.

5.1 Problem description

We consider two lumbar vertebrae, L4 and L5, where L4 is under external loading and L5 is fixed to the sacrum[1]. The two vertebrae interact through the IVD. The aim is to model the system as two interacting rigid bodies with MBS to determine the loading state and use the proposed FCM approach with weak coupling to study the elastic response of each vertebra independently.

[1] https://en.wikipedia.org/wiki/Sacrum

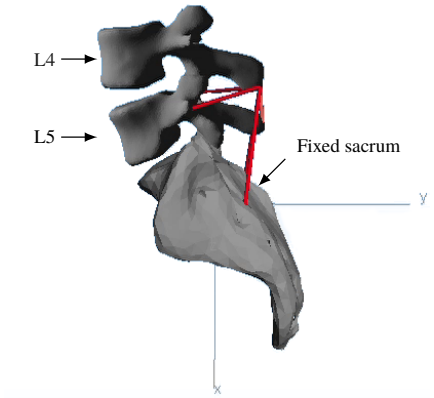

Figure 5.1: Illustration of the system from the multi-body simulation software Simpack [Das20, Ler20] .

The geometry of the vertebrae were extracted from the corresponding qCT scan of a healthy patient's spine, where the scan was performed in Rechts der Isar hospital. The iBack spine imaging research group [ERC20] performed a segmentation on the spine image, providing the geometry of individual vertebrae used in this thesis. The surface of the end plates, coupling the vertebral body with the load transferring domain, were reconstructed from the segmentation using surface regeneration tools [Gia20]. The scanned spine had a voxel resolution of $1533 \times 512 \times 81$ with a heterogeneous spacing of $0.318\,\text{mm} \times 0.318\,\text{mm} \times 2\,\text{mm}$.

The material properties were obtained from the qCT scan following the Equation (2.5) using the Hounsfield Unit. In addition to following the BMD to E mapping from Kopperdahl [KMK02], the voxels with lower BMD than $0.01\frac{g}{cm^3}$ were assigned an elastic modulus of 10^{-4} MPa. This threshold was necessary as Kopperdahl's linear model predicts positive elastic moduli starting from approximately $0.01\frac{g}{cm^3}$, as illustrated in Figure 2.3. The voxels that were assigned an elastic modulus of 10^{-4} MPa represent the voids present in cancellous parts of the vertebral body. Thus, the distribution of the assigned elastic moduli ranged from 10^{-4} MPa, representing the void voxels, to 5.0×10^3 MPa, representing stiff cortical shell. On the other hand, the elastic modulus of the helper load transferring domain was assigned as 10^7 MPa. The Poisson's ratio ν was set to 0.3, as it is commonly approximated as such. [dF15].

The intervertebral discs in MBS were modeled as non-linear springs with appropriate parameters [WP90]. The location of the spring elements were chosen to be the centroid of the intervertebral discs, determined from the scanned image. Similarly, the point of application of the external loads onto L4 was determined to represent the IVD between L4 and L3. In addition, although the dynamic effects were negligibly low, a small damping was introduced to the MB system to ensure stability during the initial loading, following [WP90].

A static compressive force of 500 N and a dynamic sinusoidal sagittal[2] moment of 10 N m was considered as a load case, as shown in Figure 5.2. The loads were applied within a time frame of

[2]https://en.wikipedia.org/wiki/Sagittal_plane

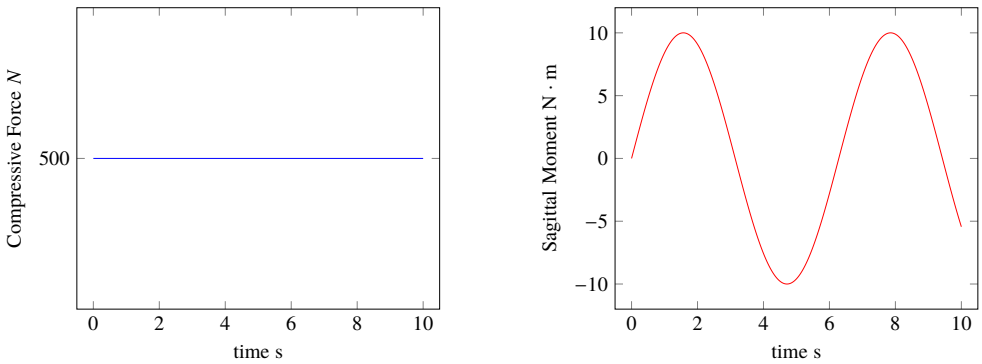

(a) Static compressive loading.

(b) Dynamic sinusoidal sagittal moment.

Figure 5.2: Load case used for MBS of L4-L5 system.

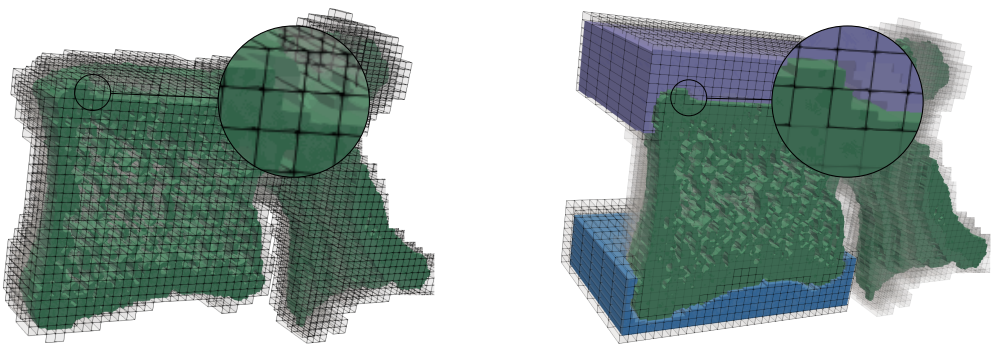

(a) The discretization of L4..

(b) Discretization of L4 together with two load transferring meshes.

Figure 5.3: The discretization scheme of L4 and its loading-interfaces viewed from sagittal section.

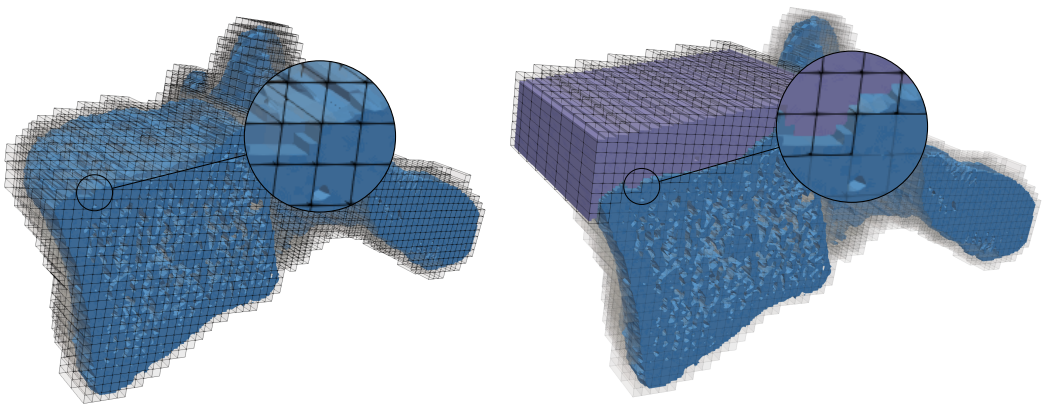

(a) The discretization of L5.

(b) Discretization of L5 together with one load transferring mesh.

Figure 5.4: The discretization scheme of L5 and its loading-interface viewed from sagittal section.

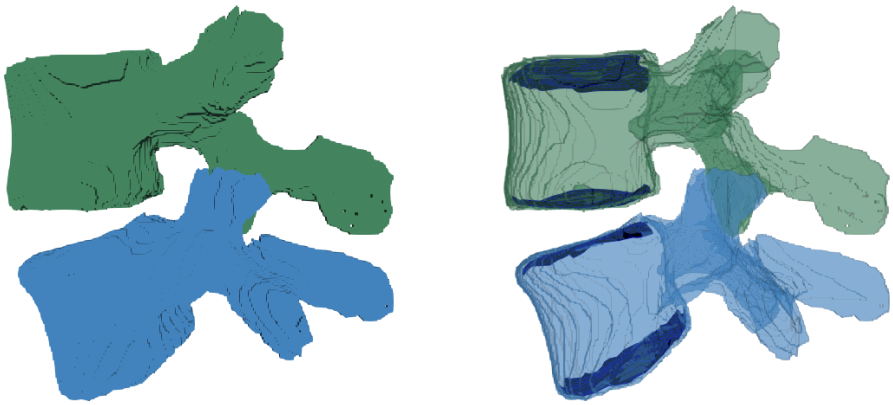

(a) Segmented L4 and L5 vertebra

(b) Segmented L4 and L5 vertebra with end-plate surfaces.

Figure 5.5: The geometry of the biomechanical system from the qCT image and reconstructed smooth end-plates.

t = 10 s with Δt = 0.01 s time increments. The computed accelerations caused a dynamic loading that was less than 1% of the spring's reaction force at all time steps, thus it was neglected following the argument in Section 4.2. Accordingly, a quasi-static analysis of elastic deformations with FCM was possible, where each time step was analyzed independently of the previous time steps.

5.2 Boundary conditions

Similar to how the loading state of the vertebrae were computed by MBS and applied in FCM, the Dirichlet conditions were arranged to be in sync between the methods. More specifically, L4 was modelled in MBS to be free to move in sagittal plane, which corresponded to restraining only rigid body modes in FCM. Furthermore, MBS modelled L5 as fixed to the sacrum, analogously it was fixed along its inferior end-plate in FCM. The Dirichlet conditions were weakly enforced following the penalty approach highlighted in Section 2.1. In case of L5, the reconstructed triangulation of the inferior end-plate surface was used to integrate the Dirichlet penalty term. On the other hand, L4 was constrained point-wise where only the cells associated with the constrained points were evaluated to determine the penalty term. To this end, the penalty parameter was selected as $\beta_D = 10^{15}$ and the α parameter was set to 10^{-8}.

The Neumann conditions were applied using the approach introduced in Section 2.2.1, where the material interface was taken as the end-plate surfaces of the vertebrae. Special attention was put into ensuring the smoothness and geometrical accuracy of the reconstructed surfaces. Accurate integration over the end-plates is especially critical as the workflow depends on the loads being correctly "transferred" to the vertebral bodies. To ensure integration quality, the surface triangulations of the end-plates were intersected with the finite cell grid and further partitioned.

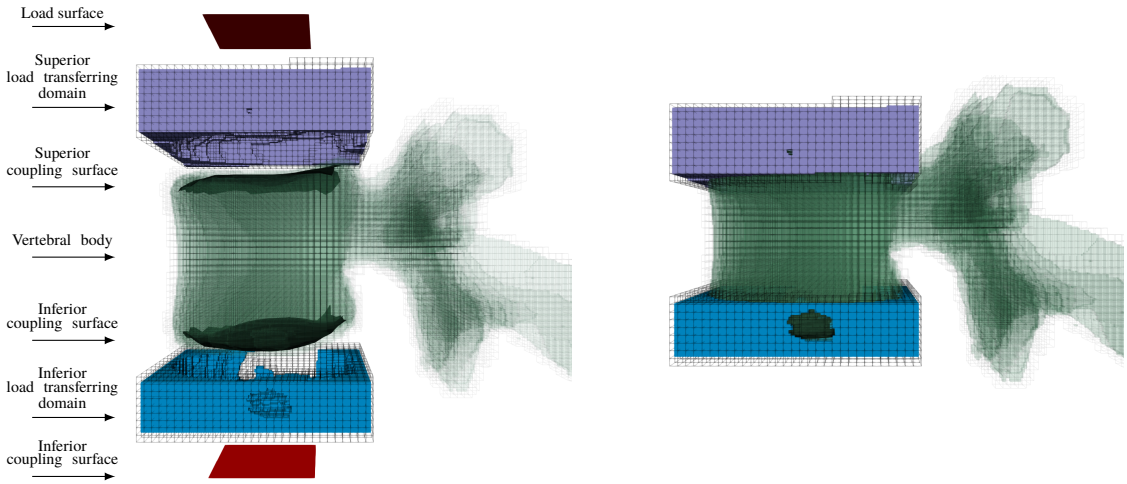

(a) The components piecing together the discretization.

(b) The discretization of L4 with its superior and inferior loading interfaces.

Figure 5.6: The parts composing the discretization of L4.

5.3 Discretization

5.3.1 Discretization of vertebrae

Although the two vertebrae interact in MBS, they were considered completely independent in FCM. The overall geometry definition and meshing procedure were, however, similar. The voxel definition of the vertebral geometry was attained as described in Section 5.1. Next, a voxel resolution for the cells was chosen as following the description in Section 2.1.1. For this application the cell voxel resolution was set to $v = 4$, meaning each finite cell potentially embodies $4 \times 4 \times 4$ voxels. This resolution was found to be a good trade-off between numerical accuracy and available computational resources. Figures 5.3a, 5.4a, 5.6 and 5.7 illustrate the resulting discretizations.

5.3.2 Discretization of load transferring domain

The load transferring domains were employed to apply the external loads on the superior end-plate of L4 and to apply the reaction forces developed on the inferior and the superior end-plates of L4 and L5, respectively, as depicted in Figures 5.8 and 5.9. The domains were located between the vertebral body and the centroid of the corresponding IVD. Additionally, the surface normal vectors of the load transferring domains were taken as the normal vector from its' IVD. The discretization of the vertebral body and the load transferring domain has the same cell dimensions, as illustrated in Figures 5.3b and 5.4b. Note that the inferior end-plate of L5 was not under load, but it was used to apply a homogeneous Dirichlet condition. Thus, L5 had only one load transferring domain in comparison to L4, which had two load transferring domains, as shown in Figures 5.6 and 5.7.

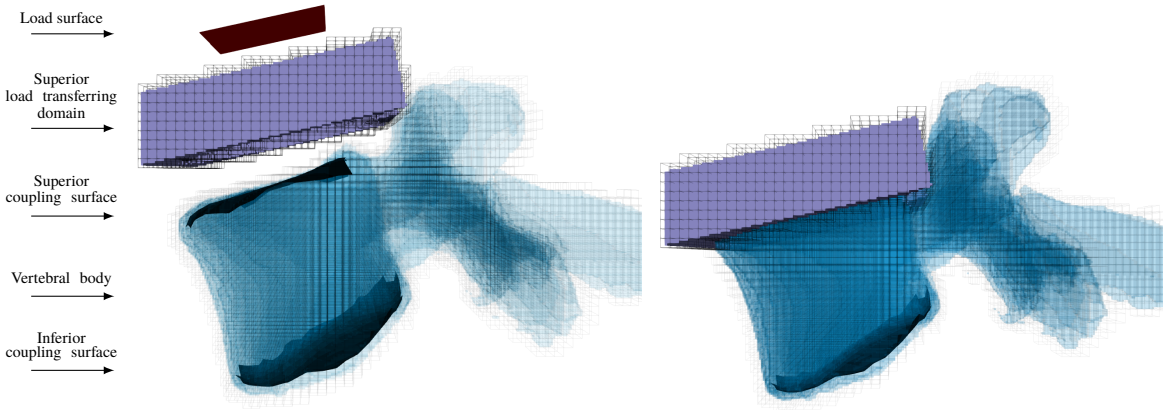

(a) The components piecing together the discretization.

(b) The discretization of L5 and its superior loading interface.

Figure 5.7: The parts composing the discretization of L4.

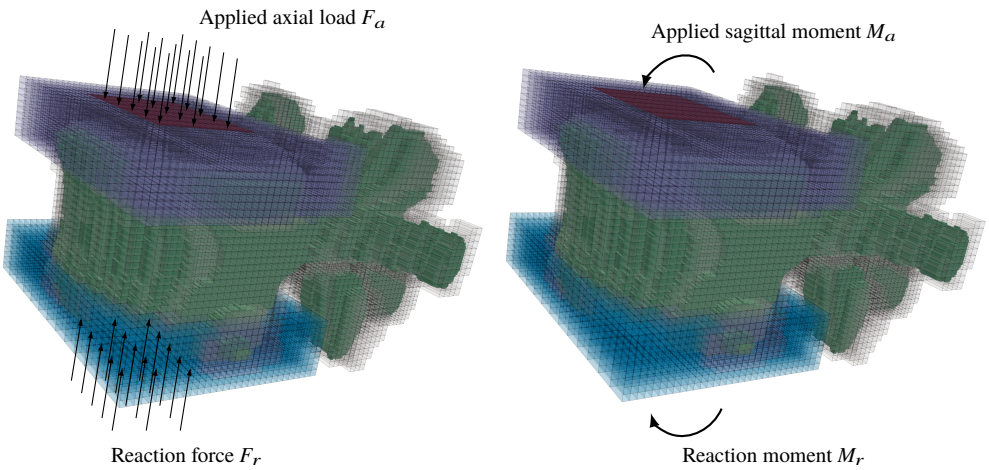

(a) The positive axial load on L4.

(b) The positive sagittal moment on L4.

Figure 5.8: The application of load cases on L4.

Finally, finite cell grids with a size of 10,970 and 13,414 cells were set up for vertebral bodies L4 and L5, respectively. Additional 5,521 and 3,165 cells were created for the load transferring domains of L4 and L5, respectively. With a polynomial degree $p = 4$ and without any further refinement, the three discretizations attributed to L4 had 900 thousand degrees of freedom in total, whereas L5 with its two grids had a total of 660 thousand degrees of freedom.

A key attribute of the FCM workflow, as emphasized in the introduction, was the ease of automation. Setting the problem up for a different patient requires a new set of inputs specific to the patient, such as the qCT image of the patient's spine. The FCM can handle the changes in the geometry, the material and the boundary conditions without significant manual intervention.

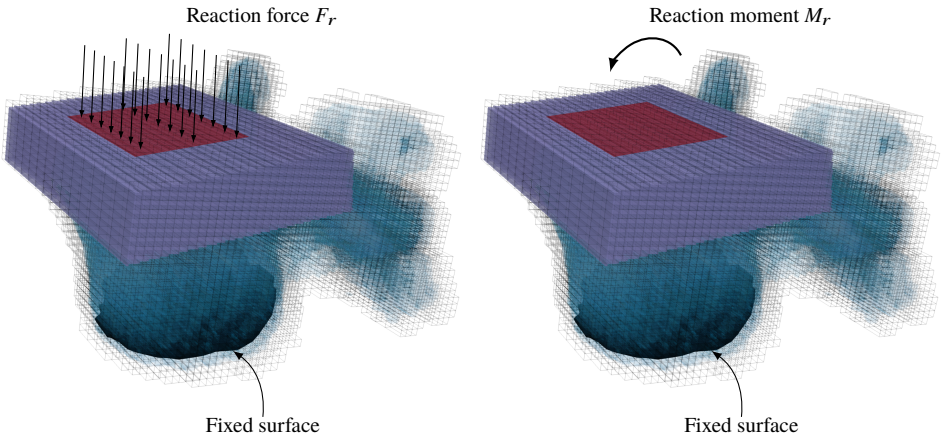

(a) The positive axial load on L5.

(b) The sagittal moment on L5, from rotational spring's reaction.

Figure 5.9: The application of load cases on L5.

Indeed, as long as the following input is provided, the FCM workflow can be generalized to analyze any vertebra.

- The segmented qCT scan of the spine.
- The triangulated end-plate surfaces of the vertebrae.
- The loading state at each time step, provided by MBS.
- The type of Dirichlet condition, in sync with MBS.

In addition to the essential input above, FCM specific parameters are also required, e.g. α , penalty parameters, etc., however they demand minimal manual decision making. In essence, the FCM enables an approach that is almost entirely agnostic to the geometry, involving no discretization of a complex 3D body such as a vertebra. A surface triangulation from the identified end-plate points is nevertheless necessary, yet unlike a volumetric discretization, the surface triangulation is uncomplicated and well-suited for automation.

5.4 Numerical results

For the solution of the resulting system of equations, the parallel sparse direct solver Intel® MKL PARDISO [Int20] was used. The decision to employ a direct solver was twofold. Firstly, FCM with its α indicator function and penalty approach suffers from conditioning problems. The preconditioning methods tuned for the mentioned conditioning problems are actively being developed, making iterative solvers a viable option [JdPE+19]. Secondly, perhaps the more compelling aspect is based on the observation that between the time steps of the linear quasi-static analysis, only the loading conditions change, whereas all the other aspects, e.g. materials, Dirichlet conditions and geometry remain the same. More specifically, once the stiffness matrix is assembled during the first time step, it need

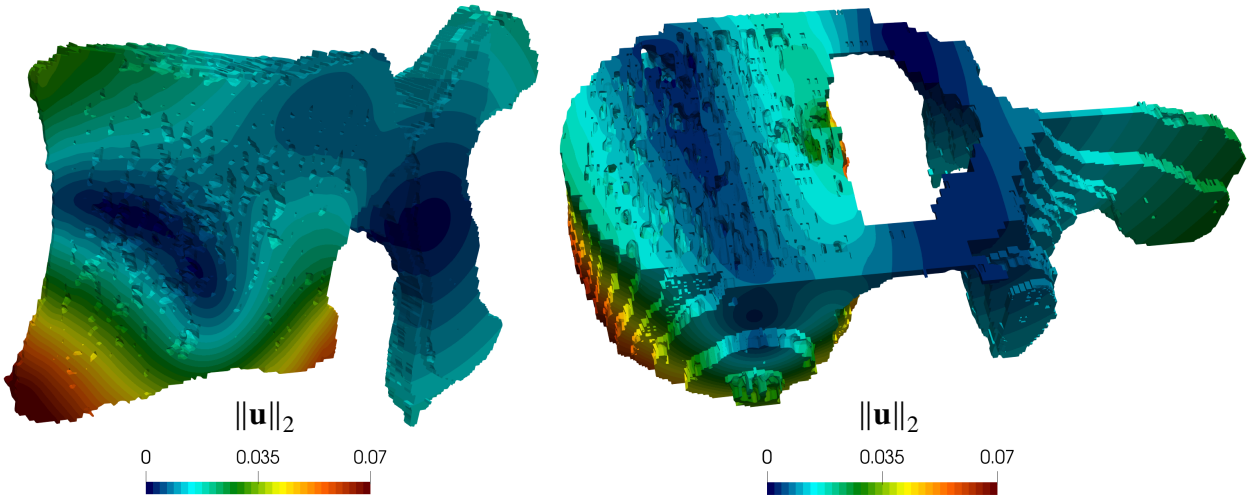

(a) Sagittal section. **(b)** Axial section.

Figure 5.10: Displacements on L4 at $t = 1.6$ seconds, in mm.

not be computed again for the time steps ahead. Thus, during the solution phase of the first time step, the factorization of the stiffness matrix was cached and reused in later time steps. To put it in perspective, the quasi-static analysis of L4 with the six-core Intel® Core™ i5 9600K @ 4.6 GHz CPU took around 3 minutes to integrate the stiffness matrix and 3 minutes to solve during the first time step , whereas the subsequent time steps took around 3 seconds to solve the cached factorization with iterative refinement technique [SG04]. With this optimization, sampled 50 time steps with $\Delta t = 0.2$ seconds time increment were solved and post-processed on voxel level under 20 minutes for each vertebra. Notably, at least 45 GB of available memory was required to perform this analysis, where the sparsity and the symmetricity of the system matrix contributed to the relatively small memory footprint.

We consider the displacement and stress state at $t = 1.6$ seconds, where a high positive sagittal moment is present. Due to the positive direction of the applied moment at this time step, we expect high stresses near the anterior[3] side as both of the applied loads induces compressive stresses in that vicinity.

The resulting von-Mises stresses for L4 and L5 are depicted in Figures 5.12 and 5.13 for a sagittal and an axial view. All in all, the observed stress state is mechanically plausible. Previous numerical studies of similar vertebrae and load cases reported similar maximum von-Mises stresses [MAA+19, KWK13]. We observe that there are no abrupt jumps in stresses between the voxel boundaries and that the stresses are mostly resolved except in rare locations. High stresses are present on voxels representing the cortical shell, showing good agreement with the general stress distribution of vertebrae under axial load and bending [MAA+19, KRAA19]. The inside of the vertebral body, filled with spongy-porous cancellous bone, has visible variations in stresses due to its irregular material distribution. In

[3]https://teachmeanatomy.info/back/bones/vertebral-column/

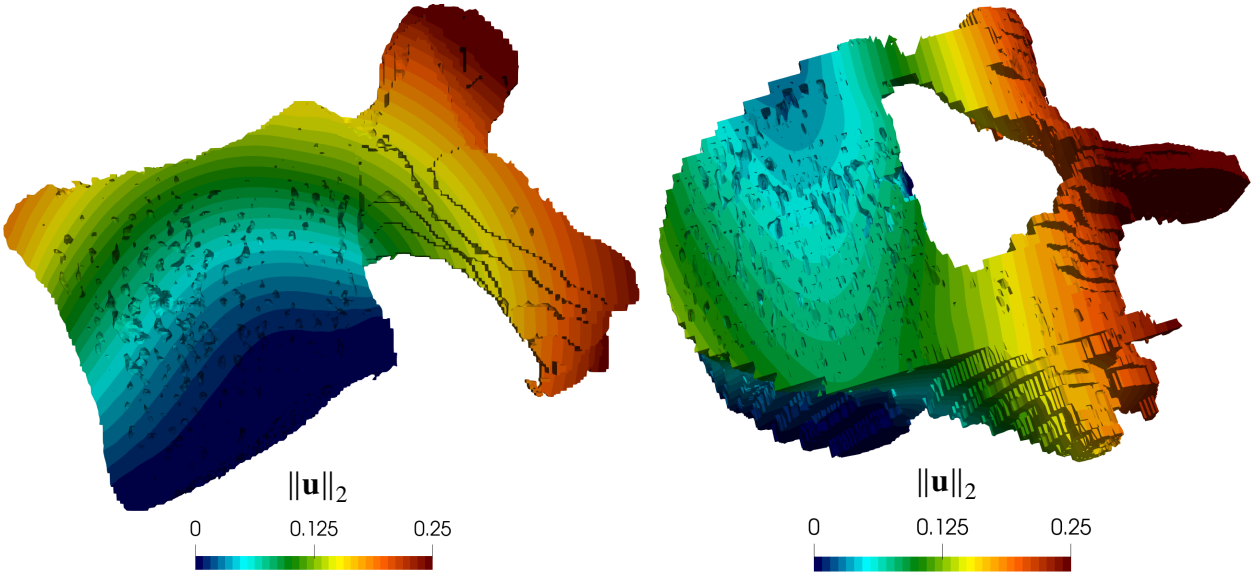

(a) Sagittal section. **(b)** Axial section.

Figure 5.11: Displacements on L5 at $t = 1.6$ seconds, in mm.

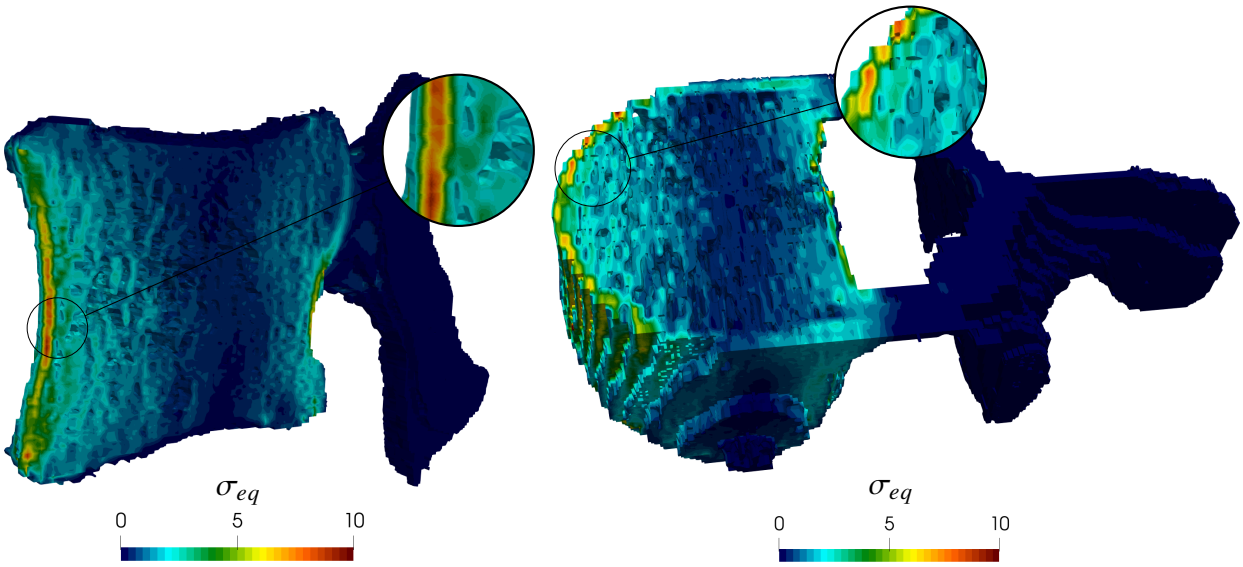

(a) Sagittal section. **(b)** Axial section.

Figure 5.12: Von-Mises stresses on L4 at $t = 1.6$ seconds, in MPa.

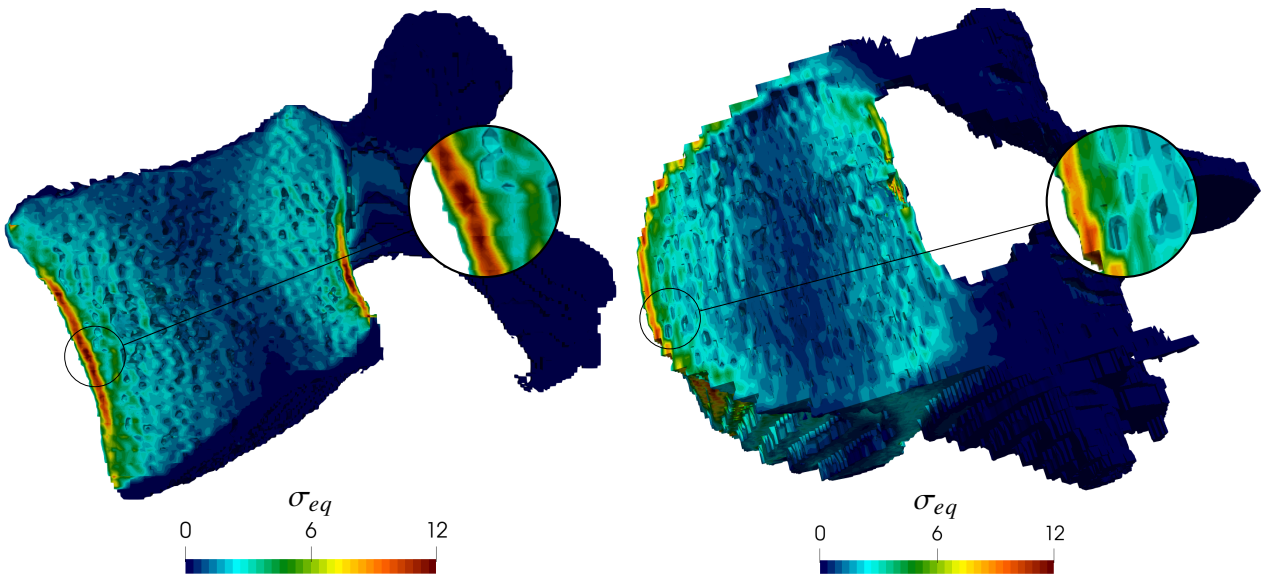

(a) Sagittal section. **(b)** Axial section.

Figure 5.13: Von-Mises stresses on L5 at t = 1.6 seconds, in MPa.

addition, higher stresses occur in the vicinity of the pedicle[4]-vertebral body intersection due to the sharper geometrical features.

As discussed in Section 5.3, a homogeneous discretization without any refinement strategy was adopted in this thesis. In further studies, multi-level hp-refinement strategy [Zan17] can be used to improve the stress resolution on specific areas of interest, e.g. in cortical shell. This approach have been carried out in a similar setting of voxel geometry of a vertebra [EZB+17], where the stress concentrations were resolved in an efficient manner.

5.5 Preview of an enhanced model

The previous sections introduced the two vertebrae system and discussed the numerical results from a combined MBS and FCM approach. Although it can be inferred that the numerical results of the two vertebrae system are mechanically plausible, a more comprehensive system considering additional vertebrae can better encapsulate the overall mechanical behavior of the lower spine. Therefore, we introduce a four vertebrae model, including the vertebrae from L2 to L5. It should be noted that the time-dependent loading conditions for this configuration were not approximated by a corresponding MBS, due to the time constraints on the thesis. Nevertheless, we consider a manufactured load case of a static moment on L2. Accordingly, this section gives a preview on the capabilities of the proposed FCM workflow for dealing with a more extensive configuration.

[4]https://www.imaios.com/en/e-Anatomy/Anatomical-Parts/Pedicle-of-vertebral-arch

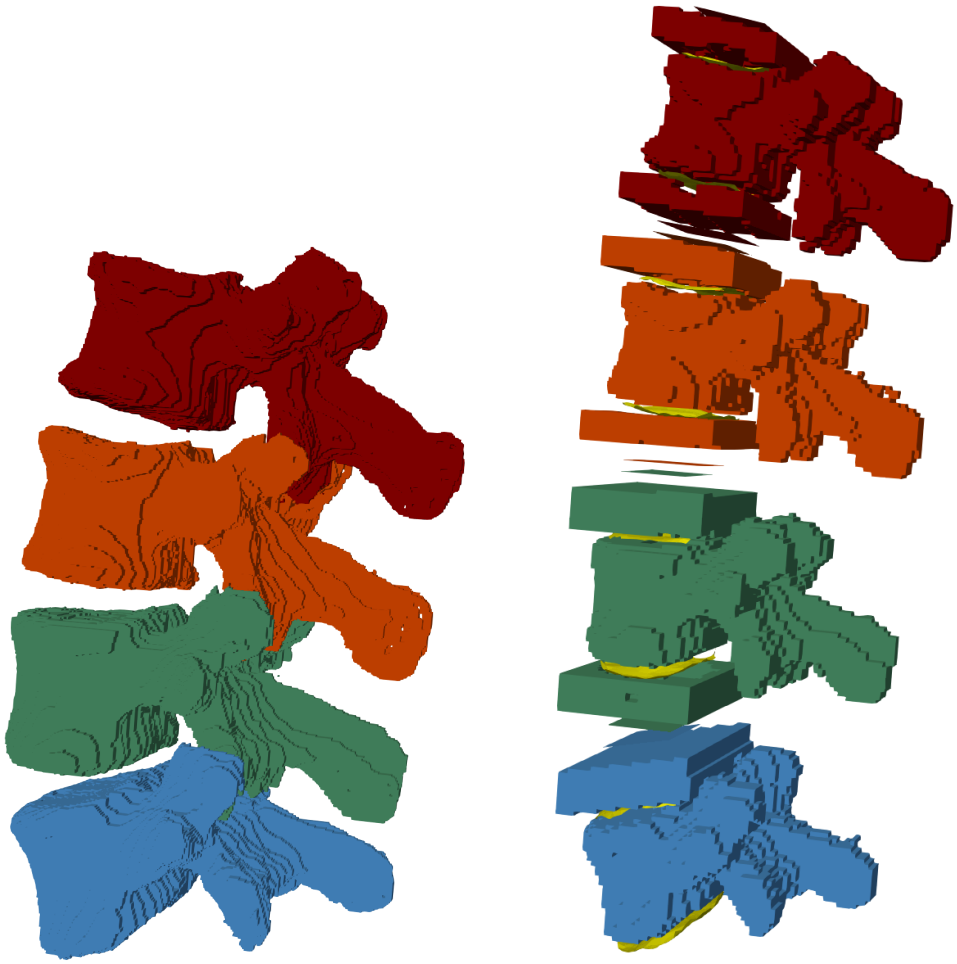

(a) The voxel geometries of L2-L5 vertebrae.

(b) The meshes, end-plate surfaces and load surfaces of L2-L5 vertebrae.

Figure 5.14: The preview model with lumbar vertebrae L2 to L5.

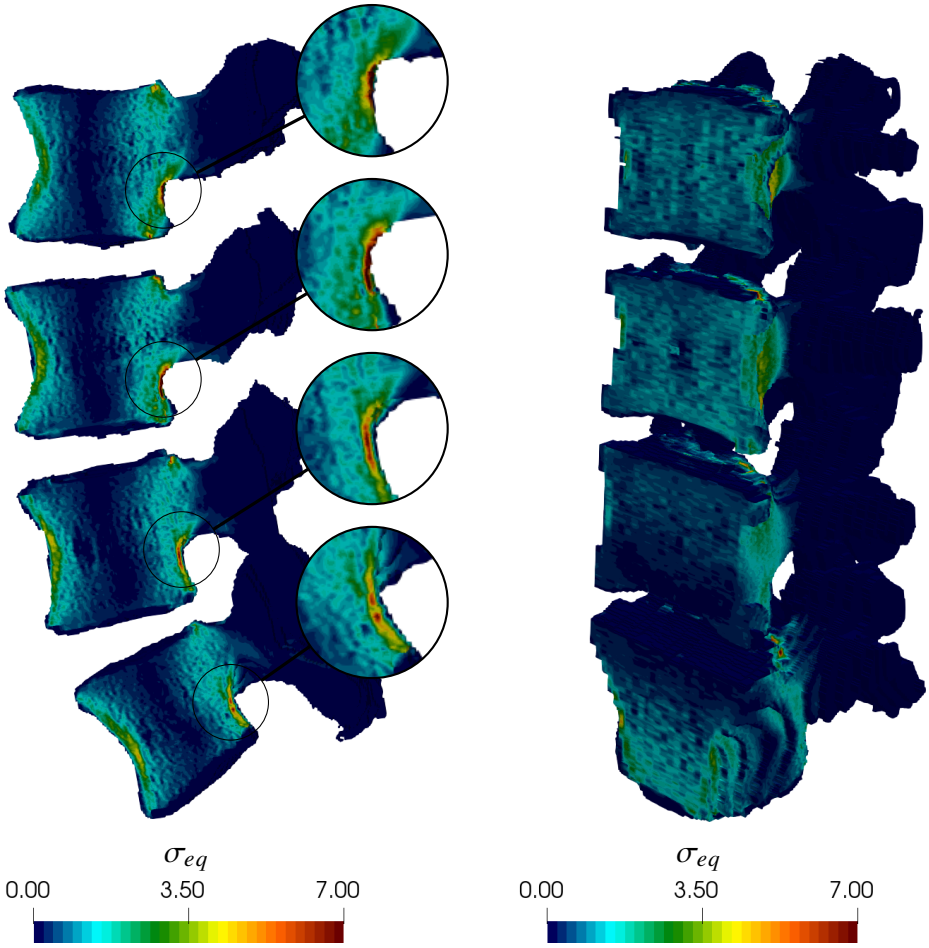

(a) The von-Mises stresses from a sagittal view. **(b)** The von-Mises stresses from an axial view.

Figure 5.15: The von-Mises stress state of the preview system in MPa, under static moment.

Figure 5.14 illustrates the problem setup, where voxel geometries of the four segmented vertebrae are shown in Figure 5.14a and the complete set of meshes and surfaces involved in the setup are presented in Figure 5.14b. The colors red, orange, green, and blue represent L2, L3, L4, and L5, respectively. The end-plate surfaces are depicted, for the sake of completeness, in yellow in Figure 5.14b. The static moment load case is assumed to exert the same positive moment of 10 N mm on each loading surface, following the positive moment sign convention established in Figures 5.8b and 5.9b. Similar to the two vertebrae system described in Section 5.1, the inferior end surface of the L5 is under weakly enforced homogeneous Dirichlet condition.

The pursued FCM workflow in this study is conceptually similar to the two vertebrae application discussed in Sections 5.3 and 5.4. For each vertebra, an independent finite cell simulation was performed. The FCM discretization was automatically generated and the application of the boundary conditions required minimal user intervention. More specifically, the required inputs were provided to the simulation framework as discussed in Section 5.3.2, where unlike Section 5.2 the boundary conditions were set up without a corresponding MBS. A polynomial degree of $p = 3$ was chosen and

the resulting discretizations of each vertebra had approximately 450 thousand degrees of freedom. The remaining parameters were kept the same as the two vertebrae system and the solver strategy was also inherited from the two vertebrae system, described in Sections 5.2 to 5.4

The key property of the setup is that the extension of the system from a two vertebrae configuration to a more comprehensive setup required marginal manual work, as the simulation framework was built with special focus on extensibility and automation. As a result, the extensibility of the setup depends solely on the availability of the required input, as discussed in Section 5.3.2.

The numerical results are presented in the form of the von-Mises stresses, depicted in Figure 5.15. Considering the pure moment load case and the heterogeneous material properties, the areas where higher stresses are observed make mechanical sense. Similar to the two vertebrae system, we can observe stress concentrations in the vicinity of the geometrically sharper features, i.e. near the pedicles. Similar conclusions regarding the regions of higher stress are documented in the literature [SGK+18, ZMBA16].

6

Summary, conclusion and outlook

The main purpose of this thesis was to develop, verify, and apply an approach to impose point loads onto irregular surfaces, enabling a seamless integration of Multi-body Simulation (MBS) and Finite Cell Method (FCM) within the context of biomechanics. The approach was to distribute the point loads onto a regularly shaped load transferring interface and to exploit the notion of material interfaces to weakly couple the load transferring domain to the original domain. The end goal of this thesis was to motivate the use of the provided computational framework with more comprehensive and realistic spine models that can generate invaluable insights on the mechanics of the spine. To this end, we first reviewed the theoretical background of FCM and its view on material interfaces, ensuring that the approach was resting on sound analytical background. Then we analyzed the approach by examining the properties of the load transferring meshes and investigated the credibility of the approach by computing numerical examples with known analytical solutions. It was found that the proposed load application method performed almost as good as a direct application of loads for the considered load cases. Thereafter, we shifted our focus to the basic principles of MBS and subsequently studied the key aspects that allow MBS and FCM to work jointly. Subsequently, we introduced a two vertebrae system, establishing an environment to demonstrate the capabilities of the proposed workflow. We analyzed the mechanical plausibility of the results by comparing the overall behaviour and tendencies of analyzed vertebrae with similar investigations from the literature. The results were found to be mechanically sensible and the observed overall stress state was in agreement with the previous work in this area. Finally, we concluded Chapter 5 with a preview of a more comprehensive model, where we argued that the proposed framework can be extended to include more of the lumbar vertebrae without significant effort.

The inspection of the numerical results confirmed that the proposed manner of load enforcement can lead to mechanically feasible stress states. As the approach takes advantage of the readily available FCM features, it is well-suited for automated patient specific workflows. Thus, the discussed results motivate the application of the combined FCM and MBS approach in a wider context, e.g. a system with all vertebrae from the lumbar spine. A successful analysis based on the proposed workflow that considers critical sections of the spine will reveal key insights about the mechanics behind the vertebral fractures. Therefore, a natural extension of this thesis would be to incorporate a larger system capable of providing greater benefit and possibly verify the credibility of such an analysis with alternative approaches or with in-vivo experiments.

Bibliography

[Ada09] J. E. Adams. *European journal of radiology*, 71:415–424, 2009.

[AF11] Ugural C. Ansel and Saul K. Fenster. *Advanced Mechanics of Materials and Applied Elasticity*. Pearson, Berlin and New York, 2011.

[Bab73] Ivo Babuška. The finite element method with penalty. *Mathematics of Computation*, 27(122):221–228, 1973.

[Bay94] de Jalon Javier Garcia Bayo, Eduardo. *Kinematic and Dynamic Simulation of Multibody Systems*. Springer-Verlag, 1994.

[Buc04] Louis Bucciarelli. 1.050 solid mechanics. online, 2004. Massachusetts Institute of Technology: MIT OpenCourseWare, https://ocw.mit.edu.

[CHB09] J. Austin Cottrell, Thomas J. R. Hughes, and Yuri Bazilevs. *Isogeometric Analysis: Toward Integration of CAD and FEA*. Wiley, 2009.

[Das20] Dassault Systemes 3DEXPERIENCE. *Simpack*, 2020. general multibody simulation (MBS) software.

[DDR15] Monique Dauge, Alexander Düster, and Ernst Rank. Theoretical and numerical investigation of the finite cell method. *Journal of Scientific Computing*, 03 2015.

[dF15] Sofia Pedroso de Faria. Biomechanical analysis of the human lumbar spine - an experimental and computational approach. *LAETA, IDMEC*, 05 2015.

[DR11] Alexander Düster and Ernst Rank. Die finite cell methode - eine fictitious domain methode mit finiten-element ansätzen hoher ordnung. *GAMM Rundbrief*, 2:6–13, 08 2011.

[ERC20] ERC-StG iBack. *iBack, individualized treatment planning in chronic back pain patients by advanced imaging and multi-parametric biomechanical models*, 2020.

[EZB+17] Mohamed Elhaddad, Nils Zander, Tino Bog, László Kudela, Stefan Kollmannsberger, Jan Kirschke, Thomas Baum, Martin Ruess, and Ernst Rank. Multi-level hp-finite cell method for embedded interface problems with application in biomechanics. *International Journal for Numerical Methods in Biomedical Engineering*, 34, 12 2017.

[Fel04] Carlos Felippa. *Introduction to Finite Element Methods*. 2004.

[Fou04] International Osteoporosis Foundation. European parliament osteoporosis interest group and eu osteoporosis consultation panel. 2004.

[Gia20] Luigi Giaccari. *Surface Reconstruction from scattered points cloud (open surfaces)*. MATLAB Central File Exchange, 2020.

[GT99] James M. Gere and Stephen P. Timoshenko. *Mechanics of Materials - Fourth SI Edition*. Nelson Thornes, 1999.

[HAEvdB10] Jason Halloran, Marko Ackermann, Ahmet Erdemir, and Antonie van den Bogert. Concurrent musculoskeletal dynamics and finite element analysis predicts altered gait patterns to reduce foot tissue loading. *Journal of biomechanics*, 43:2810–5, 10 2010.

[Int20] Intel. *Intel MKL PARDISO*, 2020.

[JdPE+19] J.N. Jomo, F. [de Prenter], M. Elhaddad, D. D'Angella, C.V. Verhoosel, S. Kollmannsberger, J.S. Kirschke, V. Nübel, E.H. [van Brummelen], and E. Rank. Robust and parallel scalable iterative solutions for large-scale finite cell analyses. *Finite Elements in Analysis and Design*, 163:14 – 30, 2019.

[JS09] Mika Juntunen and Rolf Stenberg. Nitsche's method for general boundary conditions. *Math. Comput.*, 78:1353–1374, 09 2009.

[Kit20] Kitware. *Visualization Toolkit(VTK)*, 2020.

[KMK02] David L Kopperdahl, Elise F Morgan, and Tony M Keaveny. Quantitative computed tomography estimates of the mechanical properties of human vertebral trabecular bone. *Journal of Orthopaedic Research*, 20(4):801 – 805, 2002.

[KOB+14] Stefan Kollmannsberger, Ali Oezcan, Joan Baiges, Martin Ruess, Ernst Rank, and A. Reali. Parameter-free, weak imposition of dirichlet boundary conditions and coupling of trimmed and non-conforming patches. *International Journal for Numerical Methods in Engineering*, 101, 12 2014.

[KRAA19] Zeinab Kamal, Gholamreza Rouhi, Navid Arjmand, and Samer Adeeb. A stability-based model of a growing spine with adolescent idiopathic scoliosis: A combination of musculoskeletal and finite element approaches. *Medical Engineering & Physics*, 64:46 – 55, 2019.

[KWK13] Yoon Hyuk Kim, Mengying Wu, and Kyungsoo Kim. Stress analysis of osteoporotic lumbar vertebra using finite element model with microscaled beam-shell trabecular-cortical structure. *Applied Mathematics in Biomedical Sciences and Engineering*, 2013, 2013.

[KZKR16] László Kudela, Nils Zander, Stefan Kollmannsberger, and Ernst Rank. Smart octrees: Accurately integrating discontinuous functions in 3d. *Computer Methods in Applied Mechanics and Engineering*, 306:406 – 426, 2016.

[Ler20] Tanja Lerchl. Spine research group, 2020. Associate Professorship of Sport Equipment and Sport Materials.

[LKAER18] Tao Liu, Kinda Khalaf, Samer Adeeb, and Marwan El-Rich. Effects of lumbo-pelvic rhythm on trunk muscle forces and disc loads during forward flexion: A combined musculoskeletal and finite element simulation study. *Journal of Biomechanics*, 10 2018.

[LKNER18] Tao Liu, Kinda Khalaf, Sadegh Naserkhaki, and Marwan El-Rich. Load-sharing in the lumbosacral spine in neutral standing & flexed postures – a combined finite element and inverse static study. *Journal of Biomechanics*, 70:43 – 50, 2018. 2nd International Workshop on Spine Loading and Deformation.

[MAA+19] Algirdas Maknickas, Vidmantas Alekna, Oleg Ardatov, Olga Chabarova, Darius Zabulionis, Marija Tamulaitienė, and Rimantas Kačianauskas. Fem-based compression fracture risk assessment in osteoporotic lumbar vertebra l1. *Applied Sciences*, 9, 2019.

[MZZ+19] Fuhao Mo, Haotian Zhang, Siqi Zhao, Zhi Xiao, and Tang Liu. Coupling musculoskeletal dynamics and subject-specific finite element analysis of femoral cortical bone failure after endoprosthetic knee replacement. *Applied Bionics and Biomechanics*, page 8, 02 2019.

[Neg00] Mehrdad Negahban. Pure bending. online, 2000. http://emweb.unl.edu/NEGAHBAN/Em325/11-Bending/Bending.htm.

[PDR07] Jamshid Parvizian, Alexander Düster, and Ernst Rank. Finite cell method. *Computational Mechanics*, 41, 12 2007.

[Red06] J.N. Reddy. *Theory and Analysis of Elastic Plates and Shells*. 2006.

[RTT+11] Martin Ruess, David Tal, Nir Trabelsi, Zohar Yosibash, and Ernst Rank. The finite cell method for bone simulations: verification and validation. *Biomechanics and Modeling in Mechanobiology*, 11, 2011.

[Rue14] Weak coupling for isogeometric analysis of nonmatching and trimmed multipatch geometries. *Computer Methods in Applied Mechanics and Engineering*, 269:46 – 71, 2014.

[SG04] O Schenk and K. Gartner. Solving unsymmetric sparse systems of linear equations with pardiso. Technical report, Journal of Future Generation Computer Systems, 2004.

[SGK+18] Jong Ki Shin, Tae Sik Goh, Kim, Myung-Sung Kim, Keunyoung Kim, Myung Jun Shin, Seung Min Son, Hee Jin Lee, Jung Sub Lee, and Chi-Seung Lee. Stress and strain analyses of single and segmental lumbar spines based on an accurate finite element model for vertebrae. *Biomedical Research*, 29, 2018.

[SRZ+12] Dominik Schillinger, Martin Ruess, Nils Zander, Yuri Bazilevs, Alexander Düster, and Ernst Rank. Small and large deformation analysis with the p- and b-spline versions of the finite cell method. *Computational Mechanics*, 50:445–, 02 2012.

[SYY+18] Liming Shu, Ko Yamamoto, Jiang Yao, Prabhav Saraswat, Yao Liu, Mamoru Mitsuishi, and Naohiko Sugita. A subject-specific finite element musculoskeletal framework for mechanics analysis of a total knee replacement. *Journal of Biomechanics*, 77:146 – 154, 2018.

[VdJDA+13] S. Van der Jeught, J.J. Dirckx, J.R.M. Aerts, A Bradu, A.G. Podoleanu, and J.A.N. Buytaert. Full-field thickness distribution of human tympanic membrane obtained with optical coherence tomography. *J. Assoc. Res. Otolaryngol.*, 14, 2013.

[Wit08] Jens Wittenburg. *Dynamics of Multibody Systems*. Berlin-Springer, 2008.

[WP90] A. Augustus White and M. Manohar Panjabi. *Clinical Biomechanics of the Spine*. Lippincott, 1990.

[YRK+12] Zhengxiong Yang, Martin Ruess, Stefan Kollmannsberger, Alexander Düster, and Ernst Rank. An efficient integration technique for the voxel-based finite cell method. *International Journal for Numerical Methods in Engineering*, 91:457–471, 08 2012.

[Zan17] Nils Zander. *Multi-level hp-FEM, Dynamically changing high order mesh refinement with arbitrary hanging nodes*. TUM, 2017.

[ZMBA16] Samir Zahaf, Bensamine Mansouri, Abderrahmane Belarbi, and Zitouni Azari. The effect of the eccentric loading on the components of the spine. *Hematology and Medical Oncology*, 2016.

List of Figures

Declaration of Authorship

I hereby declare that the thesis submitted is my own unaided work. All direct or indirect sources used are acknowledged as references.

I am aware that the thesis in digital form can be examined for the use of unauthorized aid and in order to determine whether the thesis as a whole or parts incorporated in it may be deemed as plagiarism. For the comparison of my work with existing sources I agree that it shall be entered in a database where it shall also remain after examination, to enable comparison with future theses submitted. Further rights of reproduction and usage, however, are not granted here.

This paper was not previously presented to another examination board and has not been published.

München, 31. March 2020

Oguz Oztoprak

Oguz Oztoprak
Arcisstraße 21 1
D-80933 München München
e-Mail: oguz.oztoprak@tum.de